

Direct Numerical Simulations of Magnetic Field Effects on Turbulent Flow in a Square Duct

R. Chaudhary, S.P. Vanka and B.G. Thomas

Department of Mechanical Science & Engineering

University of Illinois at Urbana-Champaign

Urbana, IL, USA

ABSTRACT

Magnetic fields are crucial in controlling flows in various physical processes of industrial significance. One such process is the continuous casting of steel, where different magnetic field configurations are used to control the turbulent flow of steel in the mold in order to minimize defects in the cast steel. The present study has been undertaken to understand the effects of a magnetic field on mean velocities and turbulence parameters in turbulent molten metal flow through a square duct. The coupled Navier-Stokes-MHD equations have been solved using a three-dimensional fractional-step numerical procedure. The Reynolds number was kept low in order to resolve all the scales in the flow without using a sub-grid scale turbulence model. Computations were performed with three different grid resolutions, the finest grid having 8.4 million cells. Because liquid metals have low magnetic Reynolds number, the induced magnetic field has been considered negligible and the electric potential method for magnetic field-flow coupling has been implemented. After validation of the computer code, computations of turbulent flow in a square duct with different Hartmann numbers were performed until complete laminarization of the flow. The time-dependent and time-averaged nature of the flow have been

examined through distribution of mean velocities, turbulent fluctuations, vorticity and turbulent kinetic energy budgets.

INTRODUCTION

Magnetic fields are commonly used to control flows in metal processing, MHD pumps, plasma and fusion technology, to name a few [1]. Continuous casting is one process using different types of magnetic fields in the mold to minimize defects in the final product [2]. When a magnetic field is applied to a flow field, it induces a current and the interaction of this current with the magnetic field generates a Lorentz force. This Lorentz force brakes the flow and alters the velocity field [3]. In case of turbulent flows, magnetic fields can relaminarize the flow and alter the structure of the turbulent flow significantly [4]. Consequently the friction characteristics and mixing phenomena in turbulent flows subjected to magnetic fields can be significantly different from those without a magnetic field. Tailoring the magnetic field to alter the flow in the mold of the continuous caster of steel is a topic of significant practical interest [2].

The common methodology used in most previous studies to simulate effects of magnetic field on turbulent flows has been the Reynolds-averaged approach [4-8]. However, the fundamental difficulty with such an approach is the modeling of the effects of the magnetic field on the Reynolds stresses [4]. Specifically, it is difficult to predict the suppression of turbulence and modification of the flow structures through the time-averaged approach [4]. Since the magnetic field directly acts on the turbulent fluctuations, a more rigorous method with solution of equations for the time-dependent three-dimensional turbulent flow is required. Recently, with the significant improvement in computer speed, Direct Numerical Simulations (DNS) have become

feasible as a complementary tool to experiments [9]. In the present work, the effects of a magnetic field on turbulent flow through a square duct are studied using the DNS approach.

Extensive studies exist on DNS, Large Eddy Simulations (LES) and experiments of turbulence in a planar two-dimensional channel flow (Moin and Kim [10], Kim, Moin and Moser [11], Moser, Kim and Mansour [12], Moser and Moin [13], and Monty and Chong [14]). Relatively, a smaller number of studies have considered flow in a duct with two inhomogeneous directions [15-18]. The first DNS with two inhomogeneous directions was performed by Gavrilakis [15]. A finite difference scheme with 16 million nodes and a moderate Reynolds number of 4410 were used to study turbulent flow in a square duct. The turbulence-driven secondary flows along with the bulging of the mean streamwise velocity field were accurately predicted. The turbulent statistics at the wall bisectors were seen to agree with data in a planar channel. Huser and Biringen [16] used a time-splitting method with spectral/higher-order finite difference discretization on a staggered mesh to simulate a similar flow but in their study, the Reynolds number based upon friction velocity was higher (600 with 96x101x101 grid points). Madabhushi and Vanka [17, 18] performed LES and DNS of turbulent flow in a square duct using a mixed spectral-finite difference method. DNS at Re_τ of 260 and LES at 360 were found to predict secondary flows and turbulence statistics accurately.

The turbulent flow subjected to a magnetic field has been the subject of many previous studies [19-30]. Brouillette and Lykoudis (1967) carried out experiments in a high aspect ratio (5:1) duct and predicted laminarization under a uniform and strong magnetic field [19]. Reed and Lykoudis (1978) reinvestigated effects of magnetic field on turbulence in a 5.8:1 aspect ratio duct and

studied the effect of magnetic field on friction factor [20]. Satake, Kunugi and Smolentsev (2002) performed DNS to investigate turbulent pipe flow in a transverse magnetic field at a moderate Reynolds number of 5300 and three Hartmann numbers of 5, 10, and 20 [21]. The skin friction, velocity profiles, turbulent intensities and turbulent kinetic energy budget were studied at different circumferential directions in the pipe. At locations close to wall on the horizontal axis, the velocity profile was observed to become more rounded with Hartmann flattening seen at the top and bottom of the pipe. Lee and Choi (2001) performed DNS of flow in a channel to study the effect of magnetic field orientation on the pressure drop [22]. They considered streamwise, wall-normal and span-wise magnetic fields and found increased drag due to the Hartmann effect in the case of wall normal magnetic field. Kobayashi (2006) performed LES in a channel flow under a wall normal magnetic field [23]. Results with a Coherent Structure Smagorinsky Model (CSM) were compared with those using the Smagorinsky Model (SM) and Dynamic Smagorinsky Model (DSM). Satake, Kunugi, Takase and Ose (2006) studied the effect of magnetic field on wall bounded turbulence in a channel using DNS at a high Re of 45818 and Hartmann numbers of 32.5 and 65 [24]. A uniform magnetic field was applied normal to the wall and various turbulence quantities were analyzed. Large scale structures were found to decrease in the core of the channel. Therefore, the difference between production and dissipation in the turbulent kinetic energy was found to decrease upon increase of Hartmann number in the central region of the channel. Boeck et al [25] performed DNS studies of the effect of the wall normal magnetic field on a turbulent flow in a channel at different Reynolds and Hartmann numbers. The three-layer near wall structure consisting of viscous region, logarithmic layer and plateau were reported at higher Hartmann numbers. These structures were reported signifying the importance of viscous, turbulent and electromagnetic stresses on the streamwise momentum

equation. The turbulent stresses were found decaying more rapidly away from the wall than predicted by mixing-length models. Noguchi and Kasagi [26] also conducted the DNS in MHD channel flow under transverse magnetic field at $Re_\tau=150$ and $Ha=6$. The DNS databases of this as well as other calculations are maintained at <http://www.thtlab.t.u-tokyo.ac.jp/>. Krasnov et al. [27] performed DNS and LES in a channel flow under span-wise magnetic field at two Reynolds numbers (10,000 and 20,000) and Hartmann numbers varying over a wide range. The main effect of the magnetic field was seen in turbulence suppression and reduction in the momentum transfer in the wall normal direction. The centerline velocity increased while the mean velocity gradient close to wall reduced and thus reducing the drag. The coherent structures were found to be enlarged in the horizontal direction upon increasing the Hartmann number. From comparison of LES with the DNS, the dynamic Smagorinsky model was found to reproduce the changes in the flow more accurately.

Zikanov and Thess [28, 29] studied the effect of magnetic field on turbulence using DNS in a classical 3-D cube with all directions having periodic boundary conditions. At a low magnetic interaction (Stuart) number, turbulence was found to be three-dimensional and approximately isotropic while turbulence suppression was seen at large Stuart numbers (strong magnetic field).

Very recently, Kobayashi (2008) performed LES of the flow in a square duct with a transverse magnetic field. Two Reynolds numbers ($Re=5300$ and $Re=29000$) with $64 \times 64 \times 64$ and $128 \times 128 \times 128$ grids respectively were used [30]. At $Re=5300$, the Hartmann layer as well as side-wall layers were found to laminarize together at nearly the same Hartmann number. At the higher

Reynolds number ($Re=29000$), the top and bottom Hartmann layers laminarized first, followed by laminarization of the side-wall layers.

In the present work, Direct Numerical Simulations of turbulent flow in a square duct subjected to various Hartmann numbers are conducted. The flow structures and mean velocities are studied for a nominal Reynolds number around 5000. The computer code is initially validated for turbulent flow in a channel at $Re_\tau=178.12$ without applying a magnetic field with previous work of Moser et al [12]. Subsequently, simulations in a non-MHD square duct are performed at $Re=4547$ and $Re=5368$ and results from $Re=4547$ calculation are compared with Gavrilakis ($Re=4410$) [15]. Further on, the simulation of laminar flow in a square duct with a transverse magnetic field is performed and the results are compared with previously known series solutions [31]. As a last validation, simulation of a turbulent MHD channel flow is performed at $Re_\tau=150$ and $Ha=6$ and compared with Noguchi and Kasagi [26]. A magnetic field was then applied in the vertical direction of a square duct and computations with $64 \times 64 \times 128$, $80 \times 80 \times 256$ and $128 \times 128 \times 512$ cells and $1 \times 1 \times 2\pi$ and $1 \times 1 \times 16$ domain sizes were performed. Mean and RMS velocities, Reynolds shear stresses, turbulent kinetic energy budgets, and streamwise vorticity budgets are collected and analyzed. The effects of magnetic field on friction losses in the duct are also evaluated.

GOVERNING EQUATIONS FOR A MAGNETOHYDRODYNAMIC (MHD) FLOW

It is well-known that when an electrically conducting material moves through a magnetic field, an electric current is induced. This induced electric current interacts with the magnetic field and produces a force ($\mathbf{J} \times \mathbf{B}$) on the flow field, called the Lorentz force. This Lorentz force brakes the

flow and therefore opposes the very mechanism that created it. The following equations mathematically describe the flow evolution for an incompressible MHD flow [32, 3].

Continuity equation:

$$\nabla \cdot \vec{v} = 0 \quad (1)$$

Momentum equations (x-, y- and z-)

$$\rho \left(\frac{\partial \vec{v}}{\partial t} + \nabla \cdot (\vec{v} \vec{v}) \right) = -\nabla p + \nabla \cdot \mu \nabla \vec{v} + \vec{F}_L \quad (2)$$

Since magnetic Reynolds number (Re_m) is less than unity in liquid metals, the induced magnetic field due to the induced electric current can be neglected. After neglecting the induced magnetic field, the electric potential method can be used to determine the current and the Lorentz force by the following equations [3].

$$\vec{F}_L = \vec{J} \times \vec{B}_0 \quad (3)$$

$$\vec{J} = \sigma \left(-\nabla \phi + \vec{v} \times \vec{B}_0 \right) \quad (4)$$

$$\nabla \cdot \vec{J} = 0 \quad (5)$$

By inserting current from Eq.(4) into the conservation of charge Eq.(5), a Poisson equation for electric potential can be derived as,

$$\nabla^2 \phi = \nabla \cdot (\vec{v} \times \vec{B}_0) = \vec{B}_0 \cdot \nabla \times \vec{v} = \vec{B}_0 \cdot \omega \quad (6)$$

Where ω is vorticity and external magnetic field is given as: $\vec{B}_0 = (B_{0x}, B_{0y}, B_{0z})$. Above given governing equations can be non-dimensionalized as follows:

$$\vec{x}^* = (x^*, y^*, z^*) = \left(\frac{x}{D_h}, \frac{y}{D_h}, \frac{z}{D_h} \right), t^* = \frac{t}{(D_h / W_b)}$$

$$\vec{v}^* = (u^*, v^*, w^*) = \left(\frac{u}{W_b}, \frac{v}{W_b}, \frac{w}{W_b} \right), \quad p^* = \frac{p}{\rho W_b^2}, \quad \vec{B}_0^* = \left(\frac{B_{0x}}{B_0}, \frac{B_{0y}}{B_0}, \frac{B_{0z}}{B_0} \right), \quad \phi^* = \frac{\phi}{(D_h W_b B_0)},$$

$$\vec{\nabla}^* = \frac{\partial}{\partial x^*} i + \frac{\partial}{\partial y^*} j + \frac{\partial}{\partial z^*} k$$

The non-dimensionalized continuity and momentum equations can be written as;

$$\nabla \cdot \vec{v}^* = 0 \tag{7}$$

$$\frac{\partial \vec{v}^*}{\partial t^*} + \nabla^* \cdot (\vec{v}^* \vec{v}^*) = -\nabla^* p^* + \frac{1}{\text{Re}} \nabla^* \cdot \nabla^* \vec{v}^* + \frac{\text{Ha}^2}{\text{Re}} (\vec{J}^* \times \vec{B}^*) \tag{8}$$

$$\nabla^{*2} \phi^* = \nabla^* \cdot (\vec{v}^* \times \vec{B}_0^*) \tag{9}$$

$$\vec{J}^* = -\nabla^* \phi^* + \vec{v}^* \times \vec{B}_0^* \tag{10}$$

There are essentially two independent non-dimensional parameters (Reynolds and Hartmann numbers) that govern the flow field and are defined based upon hydraulic diameter (D_h) and bulk axial velocity (W_b) as,

$$\text{Re} = \frac{D_h W_b}{\nu}, \quad \text{Ha} = D_h B_0 \sqrt{\frac{\sigma}{\rho \nu}} \tag{11}$$

PHYSICAL DOMAIN AND BOUNDARY CONDITIONS

Initially, for the validation purpose, the turbulent channel flows with and without MHD have been simulated and compared with previous DNS work [12, 26]. Figure 1 shows the physical and computational domain for the turbulent channel flow with other details (the mesh and domain sizes, mesh stretching, averaging time and Reynolds and Hartmann numbers etc.) on the runs given in Table. 1. The non-uniform mesh was used in the wall normal direction as per the stretching factor given below Table. 1. The streamwise and span-wise directions were considered

periodic with top and bottom walls as no-slip and insulated. In MHD channel, the magnetic field is applied in vertical direction, as given in Fig. 1. In addition to the above mentioned boundary conditions, in the MHD channel, the span-wise direction requires one more additional condition on mean electric potential gradient. For this purpose, the open-circuit condition in span-wise direction was assumed and the mean electric potential gradient as proposed by Lee and Choi [22] was implemented. In channel flow runs, a constant streamwise pressure gradient ($\partial \bar{p} / \partial z$) was fixed corresponding to the given Re_τ (178.12 and 150) and bulk Reynolds number was allowed to change.

Figure 2 presents the physical and computational domains considered for square duct in this study. Two directions of the domain are bounded by walls, whereas the main flow direction is considered to be periodic. The size of the domain is $1 \times 1 \times 2\pi$ and $1 \times 1 \times 16$ for the different meshes. For periodic boundary conditions, domain size should be at least twice the distance for which two-point velocity fluctuation correlation is zero [10]. Domain length of 2π or more seems adequate for the current case as proposed by Madabhushi and Vanka [17]. The preceding domain requirement still needs verification in MHD duct flow and therefore is also a subject of current study. The domain is discretized with $64 \times 64 \times 128$, $80 \times 80 \times 256$ and $128 \times 128 \times 512$ cells for the different cases studied. Table 2 presents various cases simulated for square duct flow in the current study with various details (like domain and mesh sizes, grid stretching, Reynolds and Hartmann number etc.) given. The non-uniform grids were used in wall normal directions with stretching factors given below Table. 2. A constant and uniform magnetic field is applied in the vertical (y-) direction. In all the runs the streamwise pressure gradient ($\partial \bar{p} / \partial z$) was fixed and the bulk Reynolds number was allowed to change. In all the square duct MHD runs, the

streamwise pressure gradient was fixed corresponding to $Re_\tau=361$. No-slip and insulated wall boundary conditions have been used for the side and top and bottom walls. Thus,

$$\begin{aligned}\vec{v}^* = 0, J_y^* = 0 &\Rightarrow \frac{\partial \phi^*}{\partial y^*} = 0 \quad (\text{top and bottom walls}) \\ \vec{v}^* = 0, J_x^* = 0 &\Rightarrow \frac{\partial \phi^*}{\partial x^*} = 0 \quad (\text{right and left walls})\end{aligned}\tag{12}$$

NUMERICAL METHOD

The above coupled equations have been discretized using the Finite Volume Method (FVM) on a structured Cartesian staggered grid. Pressure-velocity coupling is resolved through the fractional step method [33] with explicit formulation of the diffusion and convection terms in the momentum equations. The method consists of the following steps.

x-momentum equation:

$$\left(\frac{\hat{u}^* - u^{*n}}{\Delta t^*} \right) = \left(\frac{3}{2} (H_{u^*}^*)^n - \frac{1}{2} (H_{u^*}^*)^{n-1} \right) - \left(\frac{\partial \bar{p}^*}{\partial x^*} \right)\tag{13}$$

$$(H_{u^*}^*)^n = \left(-\frac{\partial(u^* u^*)}{\partial x^*} - \frac{\partial(v^* u^*)}{\partial y^*} - \frac{\partial(w^* u^*)}{\partial z^*} + \frac{1}{Re} \left(\frac{\partial^2 u^*}{\partial x^{*2}} + \frac{\partial^2 u^*}{\partial y^{*2}} + \frac{\partial^2 u^*}{\partial z^{*2}} \right) \right)^n$$

y-momentum equation:

$$\left(\frac{\hat{v}^* - v^{*n}}{\Delta t^*} \right) = \left(\frac{3}{2} (H_{v^*}^*)^n - \frac{1}{2} (H_{v^*}^*)^{n-1} \right) - \left(\frac{\partial \bar{p}^*}{\partial y^*} \right)\tag{14}$$

$$(H_{v^*}^*)^n = \left(-\frac{\partial(u^* v^*)}{\partial x^*} - \frac{\partial(v^* v^*)}{\partial y^*} - \frac{\partial(w^* v^*)}{\partial z^*} + \frac{1}{Re} \left(\frac{\partial^2 v^*}{\partial x^{*2}} + \frac{\partial^2 v^*}{\partial y^{*2}} + \frac{\partial^2 v^*}{\partial z^{*2}} \right) \right)^n$$

z-momentum equation:

$$\left(\frac{\hat{w}^* - w^{*n}}{\Delta t^*} \right) = \left(\frac{3}{2} (H_{w^*})^n - \frac{1}{2} (H_{w^*})^{n-1} \right) - \left(\frac{\partial \bar{p}^*}{\partial z^*} \right) \quad (15)$$

$$\begin{aligned} (H_{w^*})^n = & \left(-\frac{\partial(u^* w^*)}{\partial x^*} - \frac{\partial(v^* w^*)}{\partial y^*} - \frac{\partial(w^* w^*)}{\partial z^*} + \frac{1}{\text{Re}} \left(\frac{\partial^2 w^*}{\partial x^{*2}} + \frac{\partial^2 w^*}{\partial y^{*2}} + \frac{\partial^2 w^*}{\partial z^{*2}} \right) \right)^n \\ & \left(\frac{\partial}{\partial x^*} \left(\frac{\partial p^{*n}}{\partial x^*} \right) + \frac{\partial}{\partial y^*} \left(\frac{\partial p^{*n}}{\partial y^*} \right) + \frac{\partial}{\partial z^*} \left(\frac{\partial p^{*n}}{\partial z^*} \right) \right) = \frac{1}{\Delta t^*} \left(\frac{\partial(\hat{u}^*)}{\partial x^*} + \frac{\partial(\hat{v}^*)}{\partial y^*} + \frac{\partial(\hat{w}^*)}{\partial z^*} \right) \end{aligned} \quad (16)$$

$$u^{*n+1} = (\hat{u}^*) - \Delta t^* \left(\frac{\partial p^{*n}}{\partial x^*} \right)^{n+1} \quad (17)$$

$$v^{*n+1} = (\hat{v}^*) - \Delta t^* \left(\frac{\partial p^{*n}}{\partial y^*} \right)^{n+1} \quad (18)$$

$$w^{*n+1} = (\hat{w}^*) - \Delta t^* \left(\frac{\partial p^{*n}}{\partial z^*} \right)^{n+1} \quad (19)$$

where $p^* = \bar{p}^* + p^{*n}$.

Convection and diffusion terms have been discretized using the second order central differencing scheme in space. Time integration has been achieved using explicit second order Adams-Bashforth scheme. A multigrid solver is used to solve the Pressure Poisson Equation (PPE). Neumann boundary conditions are used at the walls for the pressure fluctuations (p^*). The Electric Potential Poisson Equation (EPPE) is solved for ϕ^* also using a multigrid solver. The Lorentz force ($\vec{J}^* \times \vec{B}^*$) is then calculated and added as an explicit source term in momentum equations. All the calculations have been performed on a CPU (1.6 Ghz Itanium processor) based code written in FORTRAN except the finest calculations which have been performed by

extending CU-FLOW (A Graphic processing Units (GPUs) based code) [34] with MHD modules [35] and vorticity, TKE budgets routines.

RESULTS AND DISCUSSION

Results without the magnetic field

We now present the results of the various calculations performed in this study. First, without a magnetic field, results at $Re_\tau=178.12$ with $128 \times 128 \times 512$ grid are compared with those of Moser et al [12]. Figures 3(a) and 3(b) give the comparisons of normalized mean axial velocity and RMS of velocity fluctuations respectively. The mean axial velocity and the RMS of velocity fluctuations are found to match very closely with the DNS of Moser et al [12].

Subsequently, the results in a square duct without a magnetic field for $Re=4547$ and $80 \times 80 \times 256$ grid are compared with those of Gavrilakis [15] for a Reynolds number of 4410. Figures 4(a) and (b) give (snapshots) the instantaneous and the time-averaged flow fields, shown through contours of the streamwise velocity and cross-sectional velocity vectors. The secondary flows generated by the anisotropic turbulence stresses are clearly captured. These secondary velocities are directed from the center towards the corners and cause bulging in contours of the streamwise velocity. Figure 4(c) shows an instantaneous picture of the flow at a y^+ of 15. Regions of high and low speed streaks are clearly visible signifying the near wall sweeps and bursts in the x-z plane.

Figure 5(a) shows a comparison of the normalized mean axial velocity with results of Gavrilakis [15] at $Re=4410$. The mean axial velocity along the horizontal bi-sector from the current

simulation is found to match well with results of Gavrilakis. Figure 5(b) shows a comparison of the normalized axial velocity along the diagonal of the duct. Again, normalized velocity matched with Gavrilakis [15] closely. Figure 5(c) presents comparison of RMS of axial velocity fluctuations with Gavrilakis [15] which also match closely with each other except for a minor disagreement probably due to the slightly different Reynolds number.

Results with a magnetic field

Figure 6 shows comparisons of the normalized axial velocity with analytical series solution of Muller and Buhler [31] for a laminarized square duct flow in the presence of a strong transverse magnetic field. Here the flow was initiated with a mean axial pressure gradient ($\partial \bar{p} / \partial z$) corresponding to $Re_\tau=372$ (corresponds to bulk $Re \sim 5368$ with $64 \times 64 \times 128$ grids) (calculated based upon hydraulic diameter) and a perturbation (1% of the mean) in the three directional velocities was applied for the initial 1500 timesteps to initiate turbulence. A strong magnetic field corresponding to $Ha=60$ was then applied. The strong magnetic field was found to annihilate turbulence followed by flattening of the velocity profile close to top and bottom walls. The suppression of turbulence reduces the frictional losses but subsequent velocity flattening close to top and bottom walls supersedes this reduction and increases friction losses, thus reducing the bulk Reynolds number from ~ 5368 to 3900. The axial velocity along the horizontal bisector showed dampening of turbulence with a parabolic profile (hydrodynamic laminar profile) but the effect of velocity flattening is relatively smaller at this location. The velocity along the vertical bisector showed strong turbulence dampening followed by the velocity flattening. The axial velocity profiles match closely with the series solutions.

Figures 7(a) and 7(b) present comparisons of normalized mean axial velocity and RMS of velocity fluctuations with the DNS results of Noguchi and Kasagi (1994) at $Re_\tau=150$ and $Ha=6$ in a channel. The current mean as well as RMS of velocity fluctuations matched closely with the results of Noguchi and Kasagi [26].

Figure 8(a) shows mean axial velocities along the horizontal bisector for three grid sizes at $Ha=21.2$ and their comparison with Kobayashi's LES results ($Re=5300$, $Ha=21.2$) [30]. In these cases, flow was initiated with a mean $\partial \bar{p} / \partial z$ corresponding to $Re_\tau=361$ (calculated based upon hydraulic diameter) with a perturbation (1% of mean axial velocity) to the three directional velocities. The different grids, for the same $Re_\tau=361$, resolved magnetic field-turbulence interaction slightly differently thus causing a slight difference in frictional losses and the bulk Reynolds numbers. The mean axial velocity along horizontal bisector achieved grid independence with the $80 \times 80 \times 256$ grid. Figure 8(b) presents the mean axial velocity for the same cases along the vertical bisector. Axial velocity along this bisector with grid refinement has asymptotically approached grid independence on the finest mesh. The velocity along this bisector is seen to be more round than along the horizontal bisector. The main reason for this effect is the strong suppression of turbulence without velocity flattening at this Hartmann number close to top and bottom walls than near the side walls. Figures 8(c) and 8(d) respectively show the axial velocity along horizontal and vertical bisectors for various Hartmann numbers. Along both bisectors, mean axial velocity initially becomes more round (at $Ha=21.2$ and $Ha=22.26$) compared to the non-magnetic field case. Upon further increasing the Hartmann number (to $Ha=24.38$), the turbulence is completely suppressed. The velocity along the vertical bisector flattens and closely follows the laminar parabolic profile along the horizontal bisector.

Figures 9(a) and 9(b) respectively show the instantaneous and time-averaged velocities in a representative cross-section for $Re=5602$ and $Ha=21.2$ case. With the magnetic field, the instantaneous velocities suggest weaker fluctuations close to the top and bottom walls and in the core than closer to side walls. It can be seen that the secondary flows are significantly modified in the presence of the magnetic field. Rather than going into the corners as in the non-MHD case, the secondary flows are now directed towards the top and bottom walls close to the corners, thus lifting axial velocity contours in these regions. After impinging on the walls in the corner regions, the secondary flows return towards the center of the top and bottom walls before heading to the core of the duct from top and bottom walls. This effect due to strong secondary flow from top and bottom walls towards the core causes strong sagging in mean axial velocity close to top and bottom walls. The effect of the magnetic field on the time-mean primary and secondary velocities is weaker close to the side walls.

Figure 9(c) shows the streaky structures at a transverse plane at $Y^+=15$ for the MHD case. Streaky structures in the presence of a magnetic field are more concentrated and elongated in the streamwise direction. A similar observation of the streaky structures in a MHD pipe flow was reported by Satake et al. [21].

Figure 9(d) gives the instantaneous current density lines plotted in the cross-section for laminar and turbulent MHD duct flows. The qualitative behavior of the current density in both flows is quite similar with current being parallel to magnetic field close to side walls and perpendicular to magnetic field in the core and close to top and bottom walls. The magnitude and direction of the

Lorentz force at different locations at the cross-section are mainly controlled by the current density magnitude and direction of current density with respect to applied magnetic field. The higher current perpendicular to magnetic field causes strong Lorentz force assisting the flow close to top and bottom walls. Weak current in the opposite direction and perpendicular to the magnetic field in the core gives retarding Lorentz force in the core region. At this Hartmann number ($Ha=21.2$) in the turbulent MHD duct, although the effect of the Lorentz force is small near the side walls (because of current being almost parallel to the magnetic field), the turbulence causes the current to fluctuate and become locally perpendicular to the magnetic field, resulting in slight turbulence suppression in this region as well.

Figure 10 presents the autocorrelation of streamwise velocity fluctuations at front-mid ($0.96D$, $0.5D$) and low-mid ($0.5D$, $0.08D$) locations for $Re=5602$ and $Ha=21.2$ case. Direct spatial fluctuations as well as the temporal fluctuations (after converting them from time to length using Taylor's frozen turbulence hypothesis) have been used for calculating the spatial auto-correlations. Auto-correlations from both methods match closely within the approximation of a statistically stationary turbulent flow with turbulence intensity (w') small compared to the mean velocity. It can be seen in this figure that for both locations turbulence is de-correlated after $\sim 2.4D$. This provides an estimate of the characteristics length of the longest turbulence structure. Hence a domain length greater than twice this value ($\sim 2 \times 2.4D = 4.8D$) is sufficient to capture the longest scales of turbulence. At the locations of strong Lorentz force (i.e. low-mid ($0.5D$, $0.08D$)), the auto-correlation suggests a somewhat longer domain. A domain length of 2π is seen to be sufficient for both MHD and non-MHD cases.

Figures 11(a) and 11(b) present the RMS of axial velocity fluctuations along the horizontal and the vertical bisectors at $Ha=21.2$ respectively. As seen for the mean velocity, the grid-independence of the axial velocity fluctuations has also been obtained. Our results agree in general with Kobayashi's LES results but values in Kobayashi's LES showed over-predictions along the vertical bisector and under-predict along the horizontal bisector. We believe that the difference may be caused by the use of the SGS model in LES calculations of Kobayashi [30].

Figures 12(a) and 12(b) show the RMS of axial velocity fluctuations for different Hartmann numbers along horizontal and vertical bisectors respectively. The effect of the magnetic field in suppressing turbulence is clearly visible in the core of the duct and close to the top wall along the vertical bisector. At this Hartmann number, axial velocity fluctuations close to the top wall are suppressed by approximately 40% from the non-MHD case with a slight shift of the location of peak towards the core of the duct. The magnetic field has relatively smaller turbulence suppression in the core of the duct compared to the region close to the top wall. In a laminar duct flow, the current is purely parallel to the magnetic field close to side walls. Hence the magnetic field has no effects. However, in a turbulent duct flow, a small effect is seen close to side walls because the current can be sometimes locally perpendicular to the magnetic field due to fluctuations in the current. The effect of the magnetic field is not much different at a Hartmann number of 22.26. However, around $Ha=24$, the turbulence along both bisectors is suppressed. This finding of simultaneous suppression of turbulence along both bisectors is consistent with Kobayashi's LES calculations (at $Ha=5300$ and $Ha=21.2$) [30].

Figures 13(a) and 13(b) show the RMS of horizontal and vertical velocity fluctuations along horizontal and vertical bisectors for the various Hartmann numbers. Since the magnetic field acts strongly close to the top and the bottom walls where the current is strong and perpendicular to the field, the horizontal and vertical velocity fluctuations are suppressed strongly at these locations as well. However, close to side walls, both velocity fluctuations show weaker suppression. The variation of horizontal velocity fluctuations close to top and bottom walls is quite similar to the variation of vertical velocity fluctuations close to side walls. In the core of the duct, both horizontal and axial velocity fluctuations attain similar values.

Figures 14(a) and 14(b) show the Reynolds shear stresses ($\overline{w'u'}$, and $\overline{w'v'}$) along horizontal and vertical bisectors. Similar to the effects of the magnetic field on Reynolds normal stresses ($\overline{w'^2}$, $\overline{u'^2}$, $\overline{v'^2}$), the Reynolds shear stress ($\overline{w'v'}$) is also suppressed significantly close to top and bottom walls along the vertical bisector. Near the side walls, the suppression of $\overline{w'u'}$ is weak. Increasing Ha from 21.2 to 22.26 gives small additional suppression, especially in the region between the core and the wall.

STREAMWISE VORTICITY TRANSPORT

Streamwise vorticity is caused by the secondary velocities in the transverse plane in a turbulent non-circular duct flow [15]. Several researchers have studied the mechanism of its transport in a non magnetic duct flow with source/sinks to determine the origin of the secondary flow [15-17]. They suggested that the Reynolds stresses are responsible for the production of mean streamwise vorticity in a non-MHD duct [15-17]. Gessner and Jones [36] were the first to propose that the difference in the second derivatives of Reynolds normal and shear stresses is responsible for the

vorticity generation. Lee and Choi [22] extended the above analysis for a MHD flow. The streamwise vorticity in the case of a MHD flow has two additional terms. The first one is a second derivative of the electric potential and the second is a first derivative of a velocity component [22]. Contribution of these two additional terms is mainly decided by the magnetic field orientation and flow type. For a wall normal or span-wise magnetic field in fully developed flow, the second derivative term of the electric potential has no contribution and only the first derivative of velocity acts as an additional sink. For a streamwise directed magnetic field, only the second derivative term of the electric potential contributes to the vorticity sink. In wall normal magnetic field in a developing flow, both terms have contribution to the vorticity sink.

The vorticity transport equation for fully developed turbulent square duct flow under a transverse magnetic field (B_{0y}) (after dropping superscript “*” from non-dimensional quantities) is written as,

$$\underbrace{u \frac{\partial \bar{\Omega}_z}{\partial x}}_{\text{I}} + \underbrace{v \frac{\partial \bar{\Omega}_z}{\partial y}}_{\text{II}} = \underbrace{\frac{1}{\text{Re}} \left(\frac{\partial^2 \bar{\Omega}_z}{\partial x^2} + \frac{\partial^2 \bar{\Omega}_z}{\partial y^2} \right)}_{\text{II}} + \underbrace{\frac{\text{Ha}^2}{\text{Re}} \left(\frac{\partial \bar{u}}{\partial y} B_{0y}^2 \right)}_{\text{III}} + \underbrace{\left(\frac{\partial^2}{\partial y^2} - \frac{\partial^2}{\partial x^2} \right) (\overline{u'v'})}_{\text{IV}} + \underbrace{\frac{\partial^2}{\partial x \partial y} (\overline{u'^2} - \overline{v'^2})}_{\text{V}} \quad (20)$$

where mean streamwise vorticity is $\bar{\Omega}_z = \left(\frac{\partial \bar{v}}{\partial x} - \frac{\partial \bar{u}}{\partial y} \right)$, I is the convection of streamwise vorticity,

II is the viscous diffusion, III is the sink due to magnetic field, IV is the source/sink due to Reynolds shear stresses and V is the source/sink due to Reynolds normal stresses in the transverse plane.

Figure 15 presents the mean streamwise vorticity contours at a cross-section for a MHD and a non-MHD duct flow. Regions of positive and negative values signify the direction of rotation of secondary flows with mirror images on both sides of the diagonal bisectors signifying the secondary flows entering into the corners and exiting parallel to the side walls. The magnetic field is found to dampen the streamwise vorticity (secondary flows) across the whole cross-section and the dampening is proportional to the first derivative of horizontal velocity in vertical direction (Eq-20). The regions of high vorticity close to top and bottom walls are elongated due to vertical magnetic field acting on a strong vertical derivative of horizontal velocity and making vortices larger in this region. Exact contributions of the magnetic field to streamwise vorticity are presented in Fig. 16 which gives various budgets of mean streamwise vorticity. Convection is mainly dominant in the regions of strong vorticity gradients and secondary velocities. Since diffusion is governed by the Laplacian of the vorticity it is seen to have larger values between regions of low and high vorticity close to the walls. Second derivatives of Reynolds shear and normal stresses give source/sink to the vorticity very close to walls in the corners. Source terms caused by Reynolds shear and normal stresses are of the same order but are of opposite sign. This finding is consistent with previous works of Gessner and Jones [36], and Madabhushi and Vanka [17] in a non-magnetic duct flow. The effect of shear stress is limited to small regions compared to those of normal stresses especially close to top and bottom walls. The magnetic field makes the Reynolds normal stress terms spread in the region of elongated vorticity to act as a source there and thus an indirect effect of magnetic field on vorticity production via Reynolds normal stresses in MHD duct. The magnetic field combined with the vertical derivative of horizontal velocity acts as a sink to dampen the vorticity close to the top and bottom walls. It is necessary to note that the vorticity source caused by the magnetic field is negatively correlated

with the velocity derivative used to define vorticity (i.e. $\bar{\Omega}_z = \left(\frac{\partial \bar{v}}{\partial x} - \frac{\partial \bar{u}}{\partial y} \right)$ and $\frac{\partial \bar{u}}{\partial y}$ are negatively correlated). Thus the magnetic field produces a sink in streamwise vorticity.

TURBULENT KINETIC ENERGY BUDGET

The turbulent kinetic energy budgets in MHD square duct flow under the transverse magnetic field can be derived by summing three momentum equations after multiplying with u' , v' , w' and using averaging (again superscript “*” has been dropped from non-dimensional quantities).

The balance can be written as the sum of various terms as:

$$0 = \text{Convection} + \text{Viscous Diffusion} + \text{Dissipation} + \text{Pressure Diffusion} + \text{Production} + \text{Turbulent Diffusion} + \text{MHD Source} + \text{MHD Sink} \quad (21)$$

$$\text{Convection} = -u \frac{\partial k}{\partial x} - v \frac{\partial k}{\partial y} - w \frac{\partial k}{\partial z} \quad (22)$$

$$\text{Viscous diffusion} = \frac{1}{\text{Re}} \left(\frac{\partial^2 k}{\partial x^2} + \frac{\partial^2 k}{\partial y^2} + \frac{\partial^2 k}{\partial z^2} \right) \quad (23)$$

$$\text{Dissipation} = -\frac{1}{\text{Re}} \left(\frac{\partial u' \partial u'}{\partial x} + \frac{\partial u' \partial u'}{\partial y} + \frac{\partial u' \partial u'}{\partial z} + \frac{\partial v' \partial v'}{\partial x} + \frac{\partial v' \partial v'}{\partial y} + \frac{\partial v' \partial v'}{\partial z} + \frac{\partial w' \partial w'}{\partial x} + \frac{\partial w' \partial w'}{\partial y} + \frac{\partial w' \partial w'}{\partial z} \right) \quad (24)$$

$$\text{Pressure Diffusion} = - \left(\frac{\partial (p' u')}{\partial x} + \frac{\partial (p' v')}{\partial x} + \frac{\partial (p' w')}{\partial x} \right) \quad (25)$$

$$\text{Production} = - \left(\overline{u'^2} \frac{\partial \bar{u}}{\partial x} + \overline{u' v'} \frac{\partial \bar{u}}{\partial y} + \overline{u' w'} \frac{\partial \bar{u}}{\partial z} + \overline{v' u'} \frac{\partial \bar{v}}{\partial x} + \overline{v'^2} \frac{\partial \bar{v}}{\partial y} + \overline{v' w'} \frac{\partial \bar{v}}{\partial z} + \overline{w' u'} \frac{\partial \bar{w}}{\partial x} + \overline{w' v'} \frac{\partial \bar{w}}{\partial y} + \overline{w'^2} \frac{\partial \bar{w}}{\partial z} \right) \quad (26)$$

$$\text{Turbulent Diffusion} = -\frac{1}{2} \left(\frac{\partial \overline{u' u'^2}}{\partial x} + \frac{\partial \overline{u' v'^2}}{\partial x} + \frac{\partial \overline{u' w'^2}}{\partial x} + \frac{\partial \overline{v' u'^2}}{\partial y} + \frac{\partial \overline{v' v'^2}}{\partial y} + \frac{\partial \overline{v' w'^2}}{\partial y} + \frac{\partial \overline{w' u'^2}}{\partial z} + \frac{\partial \overline{w' v'^2}}{\partial z} + \frac{\partial \overline{w' w'^2}}{\partial z} \right) \quad (27)$$

$$\text{MHD Source} = \frac{Ha^2}{\text{Re}} \left(\overline{u' \frac{\partial \phi'}{\partial z}} - \overline{w' \frac{\partial \phi'}{\partial x}} \right) \quad (28)$$

$$\text{MHD Sink} = -\frac{Ha^2}{Re} \left(\overline{w'^2} + \overline{u'^2} \right) \quad (29)$$

Figure 17 shows the turbulent kinetic energy along the horizontal and vertical bisectors for $Re=5602$ and $Ha=21.2$. The magnetic field dampens the turbulent kinetic energy more strongly close to the top wall along the vertical bisector than close to the side wall along the horizontal bisector. Figure 18(a) presents the budget of the turbulent kinetic energy along the horizontal bisector. Very close to the right and left walls, turbulent kinetic energy is diffused from its peak region near the wall and is balanced by the viscous dissipation close to the wall. The diffusion of TKE also takes place towards the core but is weak in magnitude compared to the value towards the wall. Since production is governed by the mean velocity gradients and Reynolds stresses it has a maximum value in the region of peak axial normal stress. As expected, dissipation of TKE is the maximum close to the walls and falls off in the core. Most of the production of TKE is balanced by the dissipation term along the whole bisector. The source of turbulence due to MHD is caused by the correlation of velocity fluctuations with the derivative of electric potential, primarily the correlation of axial velocity fluctuations with the horizontal derivative of electric potential (i.e. both are perpendicular to applied magnetic field). The sink to turbulence by MHD is due to the Reynolds normal stresses in directions perpendicular to the field. The MHD sink term is qualitatively similar to the source but larger in magnitude thereby giving a net contribution in the reduction of TKE. This behavior of the MHD source and sink terms is consistent with the findings of Satake et al. [21] in the DNS of a MHD pipe flow. Convection and pressure diffusion terms have small contributions to the TKE budget. The qualitative behaviors of the non-magnetic terms in the budget are similar to those of a non-MHD duct but their magnitudes are different. Figure 18(b) gives the same budget along the vertical bisector.

These terms have smaller magnitudes along the vertical bisector because of the suppression of turbulence. Along this bisector, the diffusion term exhibits the same variation but is weaker in magnitude. The convection term is relatively stronger along this bisector. The source and sink terms due to MHD act in the same way along both the bisectors but are weaker along the vertical bisector. The net effect of the magnetic field is the suppression of turbulence along both the bisectors.

SUMMARY AND CONCLUSIONS

The present study has described in detail, using a DNS, the effects of a magnetic field on the turbulent flow in a square duct at a nominal Reynolds number of 5500. First, the code is validated for a turbulent flow in a non-MHD channel ($Re_\tau=178.12$) and a square duct ($Re=4547$ and $Re=5368(Re_\tau=372)$), followed by validation in a laminar MHD square duct ($Re=3900(Re_\tau=372)$, $Ha=60$) and a turbulent MHD channel ($Re_\tau=150$ and $Ha=6$) flow. Subsequently, simulations were performed for turbulent MHD flow in a square duct. Two domain sizes ($1 \times 1 \times 2\pi$ and $1 \times 1 \times 16$) and three grids ($64 \times 64 \times 128$, $80 \times 80 \times 256$, and $128 \times 128 \times 512$) have been used and mean as well as Reynolds normal stresses have been shown to achieve grid independence. For all MHD square duct runs, the simulations were performed by fixing a constant streamwise mean pressure gradient corresponding to $Re_\tau=361$ and varying the magnetic field for different Hartmann numbers. Thus the bulk Reynolds numbers varied slightly with Hartmann number depending upon the frictional losses and the effect of magnetic field on turbulence suppression and velocity flattening. Also, for different grid sizes, the resolved turbulence and magnetic field-turbulence interaction also contributed to the small changes in frictional losses and thus to the bulk Reynolds number.

The magnetic field affects the secondary flow significantly and shows strong bulging in the vertical direction close to top and bottom walls. Auto-correlation of axial velocity fluctuations suggested that a domain length of $\sim 5D$ is enough for capturing the longest scales of turbulence. The velocity along the vertical bisector is found to be more round than along horizontal bisector at $Ha=21.2$ because of stronger turbulence suppression along this bisector. Further increase in Hartmann number (at $Ha=24.38$), makes velocity flattening dominant along the vertical bisector but the profile along the horizontal bisector becomes more round due to complete turbulence suppression. Streaky structures get concentrated and elongated along streamwise direction under the influence of a transverse magnetic field. Because the electric current is strong and perpendicular to the magnetic field in the region close to top and bottom walls, the magnetic field suppresses the local turbulence. Close to the side walls the effect of magnetic field is weak due to the current being parallel to field. The Reynolds shear stress ($\overline{w'v'}$) shows strong suppression along vertical bisector than $\overline{w'u'}$ along the horizontal bisector.

Streamwise vorticity is suppressed directly by the magnetic field via the first derivative of horizontal velocity and indirectly via second derivatives of Reynolds normal and shear stresses, but more strongly via Reynolds normal stresses ($\overline{u'u'}$, $\overline{v'v'}$). The magnetic field produces a sink as well as a source to turbulent kinetic energy. Their variations along the bisectors are similar but the sink is stronger and causes a net reduction of turbulence due to a magnetic field.

ACKNOWLEDGMENTS

The authors gratefully thank Continuous Casting Consortium, Department of Mechanical Science & Engineering, University of Illinois at Urbana-Champaign, IL, for providing support

for this work. Authors also would like to acknowledge National Center for supercomputing Applications (NCSA) for providing computational resources. The assistance of Mr. Aaron Shinn in providing the non-MHD version of CU-FLOW is gratefully acknowledged.

REFERENCES

- (1) P. A. Davidson, Magnetohydrodynamics in materials processing, *Ann. Rev. Fluid Mech.*, 1999, 31, pp.273–300.
- (2) B. G. Thomas and Lifeng Zhang, Mathematical modeling of fluid flow in continuous casting: a review, *ISIJ International*, 2001, 41, 10, pp.1181-1193.
- (3) R. Moreau, *Magnetohydrodynamics.*, Kluwer Academic Publishers, 1990.
- (4) B. Knaepen and R. Moreau, Magnetohydrodynamic turbulence at low magnetic Reynolds number, *Ann. Rev. Fluid Mech.*, 2008, 40, pp. 25-45.
- (5) H. C. Ji and R. A. Gardner, Numerical analysis of turbulent pipe flow in a transverse magnetic field, *Int. J. Heat Mass Transfer.*, 1997, 40, pp. 1839–1851.
- (6) S. Kenjereš and K. Hanjalić, On the implementation of effects of Lorentz force in turbulence closure models, *Int. J. Heat Fluid Flow*, 2000, 21, pp. 329–337.
- (7) S. Smolentsev, M. Abdou, N. Morley, A. Ying, T. Kunugi, Application of the “k- ϵ ” model to open channel flows in a magnetic field., *Int. J. Eng. Sci.*, 2002, 40, pp. 693–711.

(8) S. Smolentsev and R. Moreau, Modeling quasi-two-dimensional turbulence in MHD duct flows. *Proc. 2006 Summer Program*, Stanford, CA: Cent. Turbul. Res., Stanford Univ. & NASA Ames Res. Cent, 2006, pp. 419–430.

(9) P. Moin and K. Mahesh, Direct Numerical Simulation: A Tool in Turbulence Research, *Ann. Rev. Fluid Mech.*, 1998, 30, pp. 539-578.

(10) P. Moin, and J. Kim, Numerical investigation of turbulent channel flow, *J. Fluid Mech.*, 1982, 118, pp. 341-377.

(11) J. Kim, P. Moin, and R. Moser, Turbulence statistics in fully developed channel flow at low Reynolds number, *J. Fluid Mech.*, 1987, 177, pp. 133-166.

(12) R. Moser, J. Kim, and N. Mansour, Direct numerical simulation of turbulent channel flow up to $Re_\tau=590$, *Phys. Fluid*, vol. 11, no. 4, pp. 943-945.

http://turbulence.ices.utexas.edu/MKM_1999.html

(13) R. Moser, and P. Moin, The effects of curvature in wall-bounded turbulent flows., *J. Fluid Mech.*, 1987, 175, pp. 479-510.

(14) J. P. Monty, and M.S. Chong, Turbulent channel flow: comparison of streamwise velocity data from experiments and direct numerical simulations, *J. Fluid Mech.*, 2009, 623, pp. 461-474.

- (15) S. Gavrilakis, Numerical simulation of low Reynolds number turbulent flow through a straight square duct, J. Fluid Mech., 1992, 244, pp. 101-129.
- (16) A. Huser, and S. Biringen, Direct numerical simulation of turbulent flow in a square duct, J. Fluid. Mech., 1993, 257, pp. 65-95.
- (17) R. K. Madabhushi and S. P. Vanka, Large eddy simulation of turbulence driven secondary flow in a square duct, Phys. Fluid A, 1991, 3, pp. 2734-2745.
- (18) R. K. Madabhushi and S. P. Vanka, Direct numerical simulation of turbulent flow in a square duct at low Reynolds number, Near-wall Turbulent flows, RMC So. C.G. Speziale and B. E. Launder (Editors), 1993.
- (19) E. C. Brouillette and P. S. Lykoudis, Magneto-fluid-mechanic channel flow. I. Experiment, Phys. Fluids, 1967, 10, pp. 995-1001.
- (20) C. B. Reed and P. S. Lykoudis, The effect of a transverse magnetic field on shear turbulence, J. Fluid Mech., 1978, 89, pp. 147-171.
- (21) S. Satake, T. Kunugi and S. Smolentsev, Direct numerical simulations of turbulent pipe flow in a transverse magnetic field, J. of Turbulence, 2002, 3, 020.

(22) D. Lee and H. Choi, Magnetohydrodynamic turbulent flow in a channel at low magnetic Reynolds number, J. Fluid Mech., 2001, 439, pp. 367–394.

(23) H. Kobayashi, Large eddy simulation of magnetohydrodynamic turbulent channel flows with local subgrid-scale model based on coherent structures, Phys. Fluids, 2006, 18, 4, pp. 45107-1-11,.

(24) S. Satake, T. Kunugi, Takase Kazuyuki and Ose Yasuo, Direct numerical simulation of turbulent channel flow under a uniform magnetic field for large-scale structures at high Reynolds number, Phys. Fluids, 2006, 18.

(25) T. Boeck, D. Krasnov and E. Zienicke, Numerical study of turbulent magnetohydrodynamic channel flow, J. Fluid Mech., 2007, 572, pp. 179-188.

(26) H. Noguchi, and N. Kasagi, Direct Numerical Simulation of Liquid Metal MHD Turbulent Channel Flows, (in Japanese), Preprint of JSME, No. 940-53, Nov. 1994, pp. 365-366.

(27) D. Krasnov, O. Zikanov, J. Schumacher, and T. Boeck, Magnetohydrodynamic turbulence in a channel with spanwise magnetic field, Phys. Fluids, 20, 095105 (2008).

(28) O. Zikanov and A. Thess, Direct numerical simulation of forced MHD turbulence at low magnetic Reynolds number, J. Fluid Mech., 1998, 358, pp. 299-333.

R. Chaudhary, S.P. Vanka, and B.G.Thomas, DNS of Magnetic Field Effects on a Square Duct Turbulent Flow, Continuous Casting Report, June 7, 2010.

(29) O. Zikanov, and A. Thess, Direct numerical simulation as a tool for understanding MHD liquid metal turbulence, Appl. Mathematical Modelling, 2004, 28, pp. 1-13.

(30) H. Kobayashi, Large eddy simulation of magnetohydrodynamic turbulent duct flows, Phys. Fluids, 2008, 20, 4, pp 015102-1-13.

(31) U. Muller and L. Buhler, Magneto Fluid Dynamics in Channels and Containers, Springer, Berlin, 2001, Sec. 4.2.1.

(32) G. K. Batchelor, An Introduction to Fluid Dynamics, Cambridge University Press; ISBN:0521663962

(33) F. Harlow and E. Welch., Numerical calculation of time-dependent viscous incompressible flow of fluid with free surface, Phys. of Fluids, 1965, 8, pp. 2182-2189.

(34) A. F. Shinn, S. P. Vanka, and W. W. Hwu., Direct Numerical Simulation of Turbulent Flow in a Square Duct Using a Graphics Processing Unit (GPU), AIAA-2010-5029, 40th AIAA Fluid Dynamics Conference, June 2010.

(35) R. Chaudhary, S.P. Vanka, and B.G. Thomas, Direct numerical simulations of magnetic field effects on turbulent duct flows, Proc. ASME Int. Mech. Eng. Congress (IMECE09), 2009, Nov. 13-19, Lake Buena Vista, FL.

R. Chaudhary, S.P. Vanka, and B.G.Thomas, DNS of Magnetic Field Effects on a Square Duct Turbulent Flow, Continuous Casting Report, June 7, 2010.

(36) B. F. Gessner, and J. B. Jones, On some aspects of fully developed turbulent flow in rectangular channels, J. Fluid Mech., 1965, 23, pp. 689-713.

Table. 1 Computational details for non-MHD and MHD channel cases for validation

$Re_\tau (= \delta u_\tau / \nu)$ δ : half channel width, ($D=2\delta$)	Grid ($N_x \times N_y \times N_z$)	Comp. domain	Spatial resolution ($\Delta x^+, \Delta y^+, \Delta z^+$)*	Mag. field orientation	Ha ($= B_\tau \delta \sqrt{\frac{\sigma}{\rho \nu}}$)	Averaging time**
178.12	128x128x512	$2/3\pi \times 1 \times 2\pi$	5.82, 1.40-4.86, 4.37	-	0	631
150	128x128x512	$2 \times 1 \times 6$	4.68, 1.17-4.09, 3.51	B_y	6	537

* grids have 2% stretching in y-direction for 128x128x512 mesh and uniform in x- and z-direction.

** Averaging time given in convective units (δ/W_b or $0.5D/W_b$)

Table. 2 Computational details for various cases

Re	Grid ($N_x \times N_y \times N_z$)	Comp. domain	Spatial resolution ($\Delta x^+, \Delta y^+, \Delta z^+$)**	Mag. field orientation	Ha	W_b	Averaging time****
4547	80x80x256	$1 \times 1 \times 2\pi$	2.53-5.49, 2.53-5.49, 3.76	-	0	1.031	1600
5368	64x64x128	$1 \times 1 \times 2\pi$	3.54-8.86, 3.54-8.86, 18.25	-	0	0.980	900
5457	64x64x128	$1 \times 1 \times 2\pi$	3.44-8.60, 3.44-8.60, 17.71	B_y	21.2	1.030	800
5681	80x80x256	$1 \times 1 \times 2\pi$	2.40-7.58, 2.40-7.58, 8.85	B_y	21.2	1.070	1600
3350	80x80x256	$1 \times 1 \times 2\pi$	2.40-7.58, 2.40-7.58, 8.85	B_y	24.38	0.630	720
5602	128x128x512	$1 \times 1 \times 16$	1.41-4.92, 1.41-4.92, 11.28	B_y	21.2	1.057	1600
5647	128x128x512	$1 \times 1 \times 16$	1.41-4.92, 1.41-4.92, 11.28	B_y	22.26	1.065	1600

*** grids have 2% stretching in x- and y-direction for all 80x80x256 and 128x128x512 meshes and 3% for 64x64x128 mesh with uniform in z-direction for all.

**** Averaging time given in convective units ($0.5D/W_b$)

Note: All MHD square duct runs are at $Re_\tau=361$.

Note: Re and Ha in square duct are based upon hydraulic diameter.

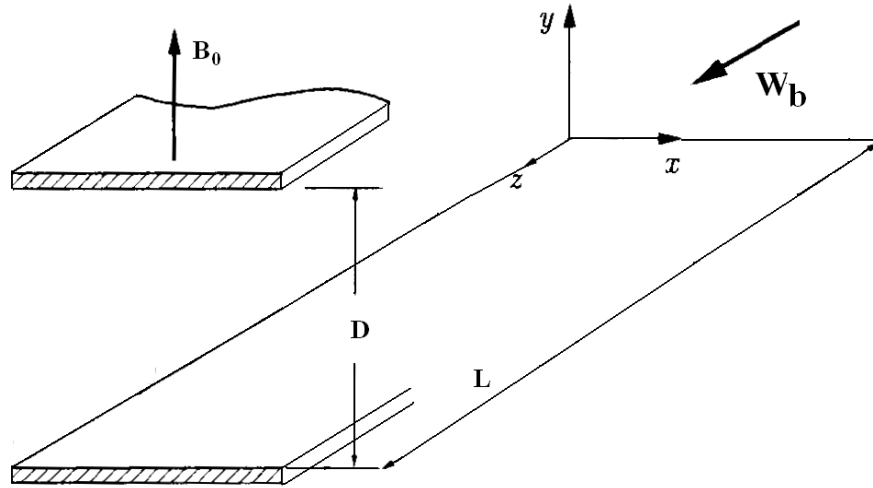


Fig. 1 Physical and computational domain of MHD and non-MHD channel

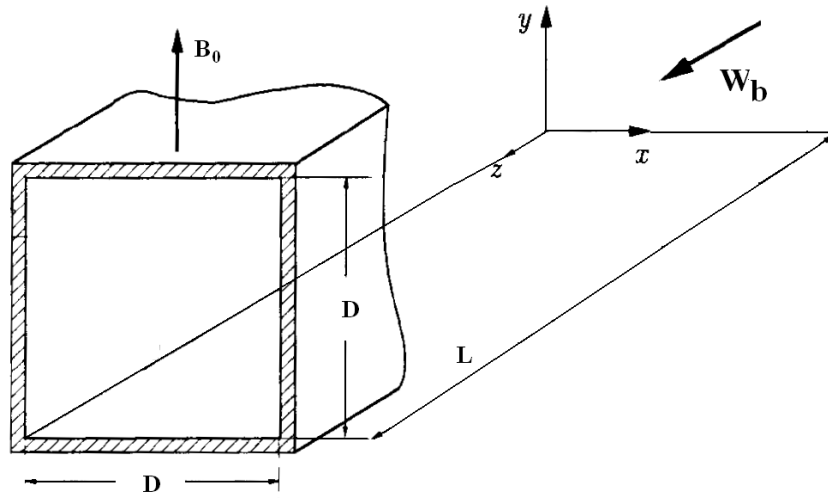


Fig. 2 Physical and computational domain of MHD and non-MHD square duct

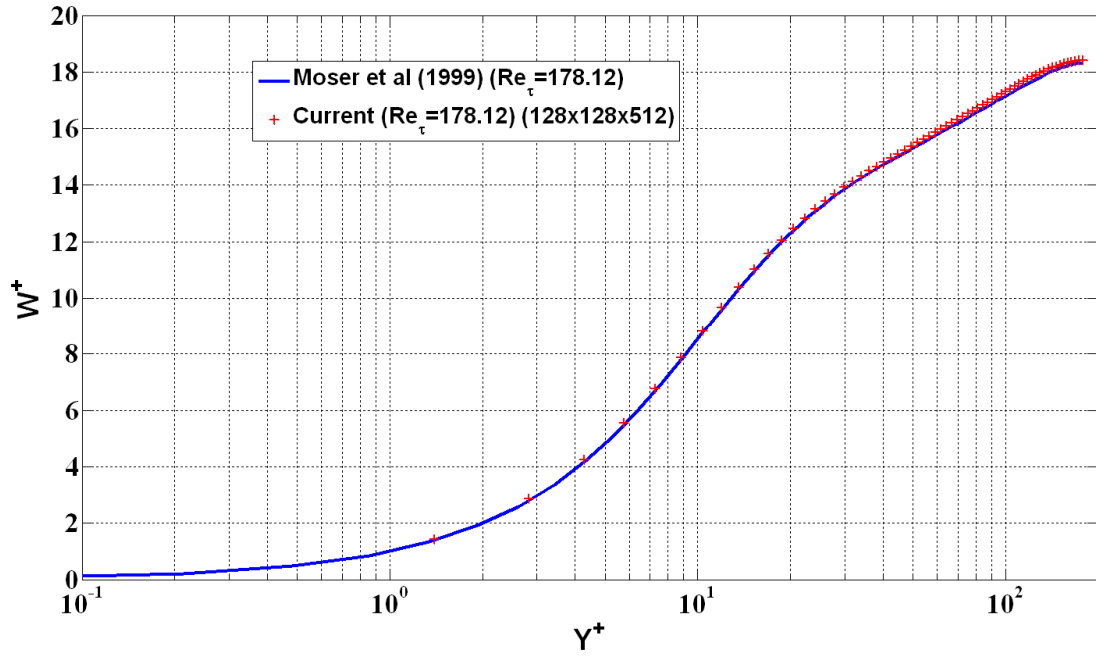


Fig. 3(a) Comparison of normalized mean axial velocity in a turbulent channel flow with the previous DNS ($Re_\tau=178.12$, Moser et al, 1999) [12]

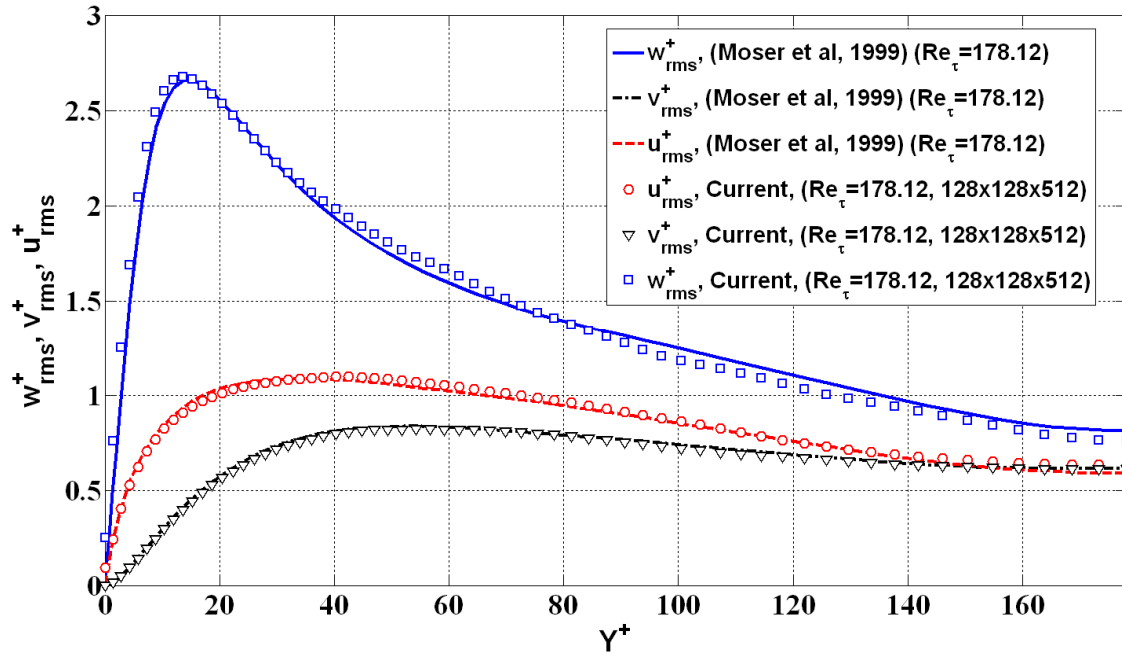


Fig. 3(b) Comparison of normalized RMS of velocity fluctuations in a turbulent channel flow with the previous DNS ($Re_\tau=178.12$, Moser et al, 1999) [12]

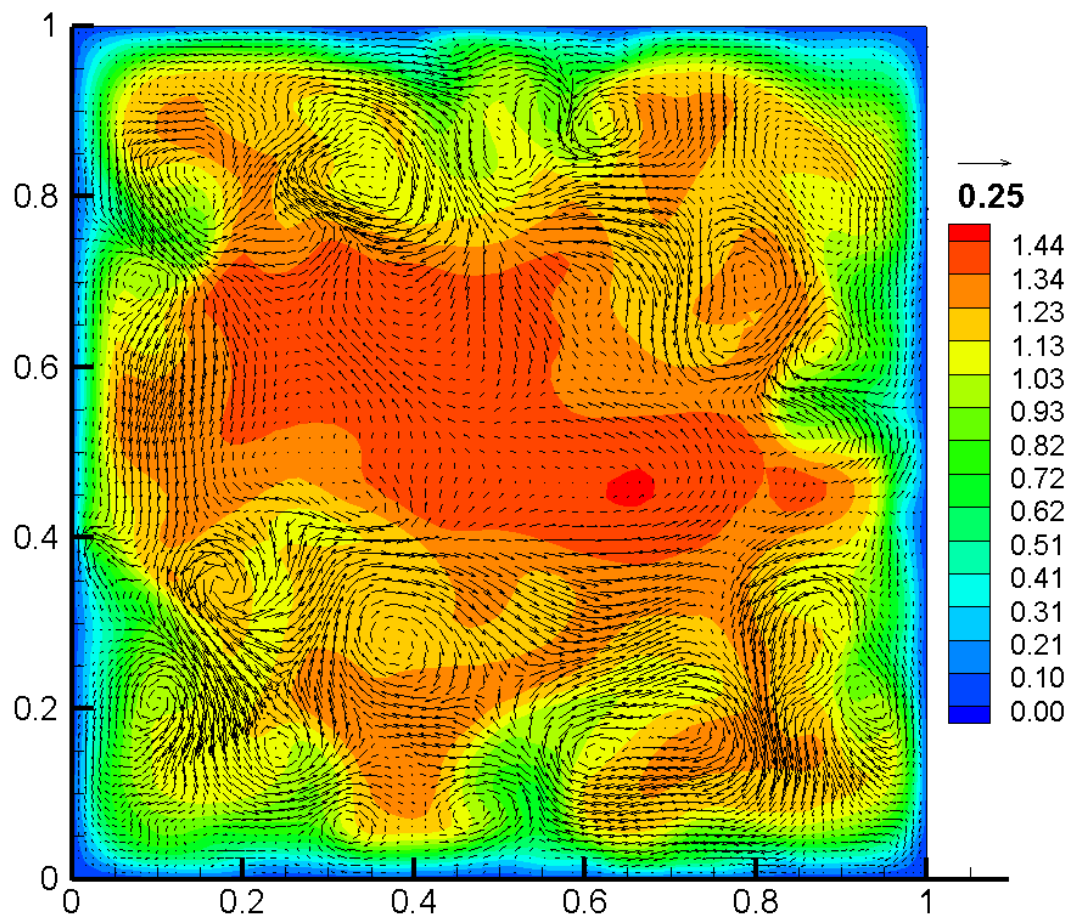


Fig. 4(a) Instantaneous axial velocity contours with secondary velocity vectors
($Re=4547$, $80 \times 80 \times 256$) for the case without a magnetic field

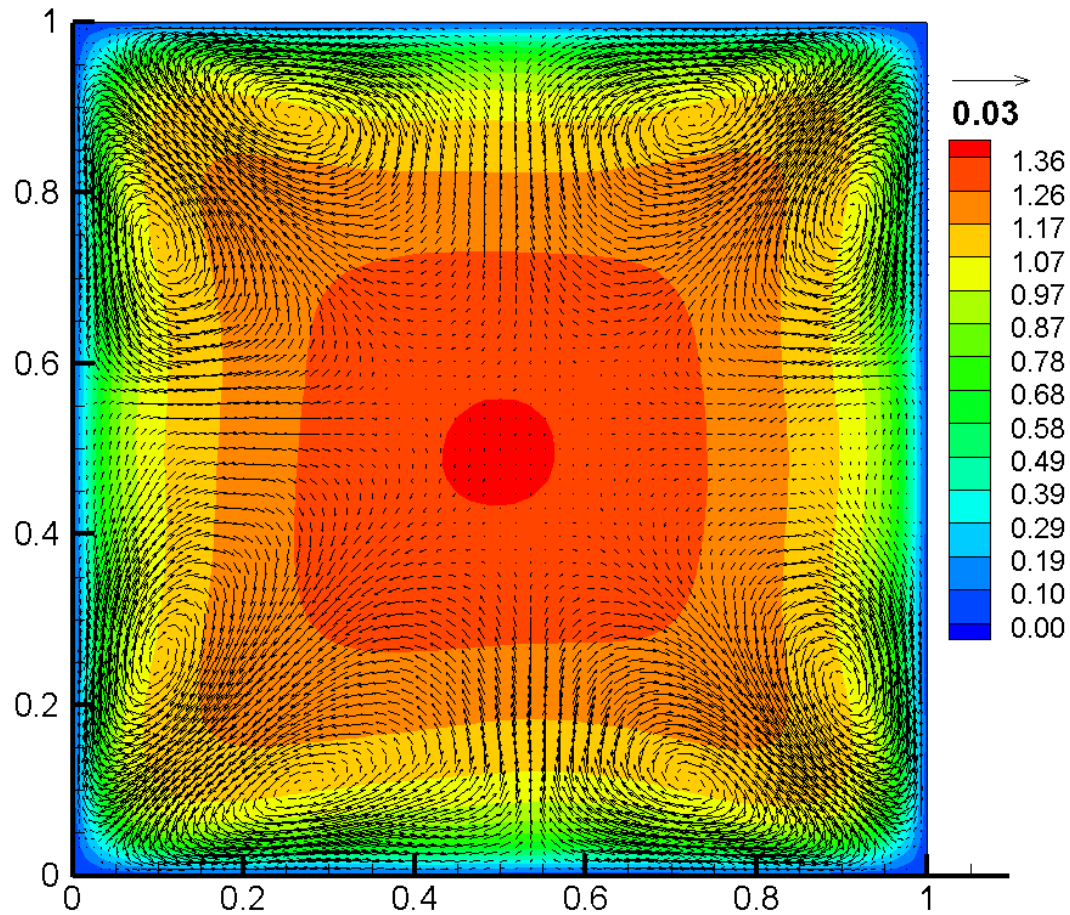


Fig. 4(b) Mean axial velocity contours with secondary velocity vectors ($Re=4547$, $80 \times 80 \times 256$) for the case without a magnetic field

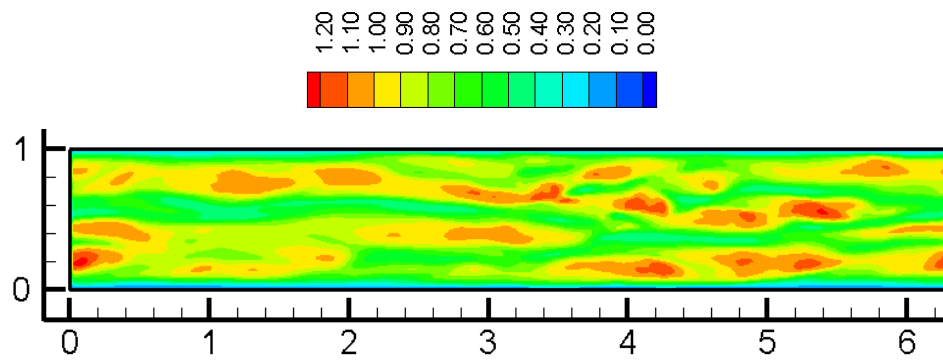


Fig. 4(c) Instantaneous velocity contours at $y^+=15$ ($Re=4547$, $80 \times 80 \times 256$)

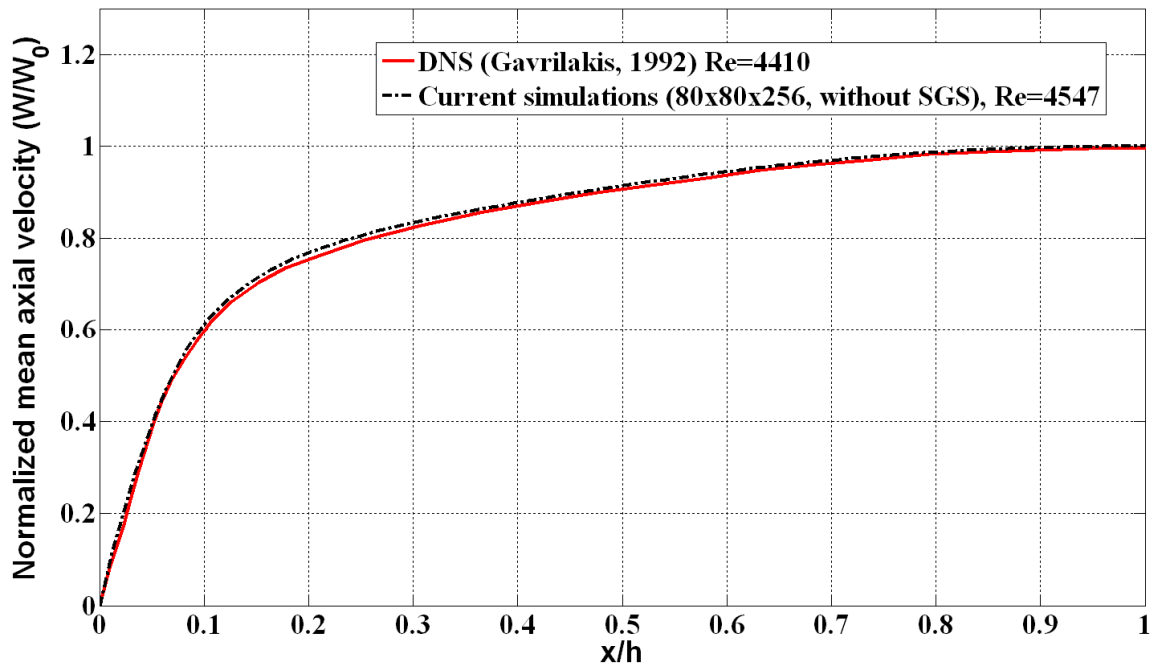


Fig. 5(a) Mean velocity comparison along horizontal bisector with Gavrilakis [15]

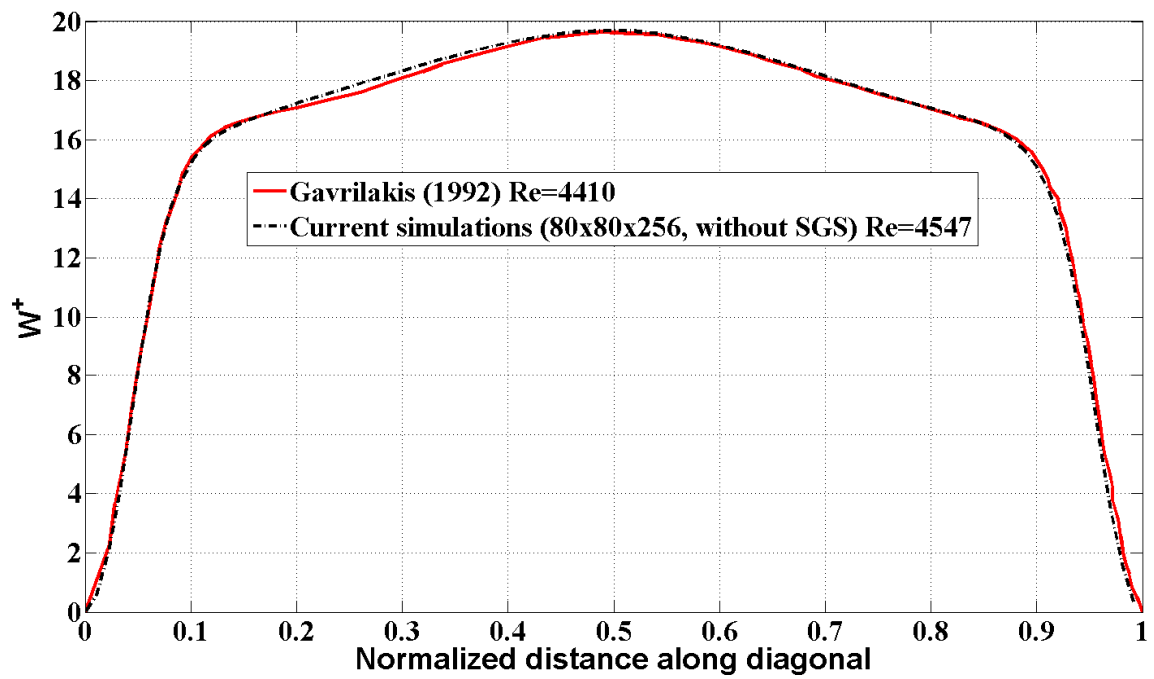


Fig. 5(b) Mean velocity comparison along diagonal with Gavrilakis [15]

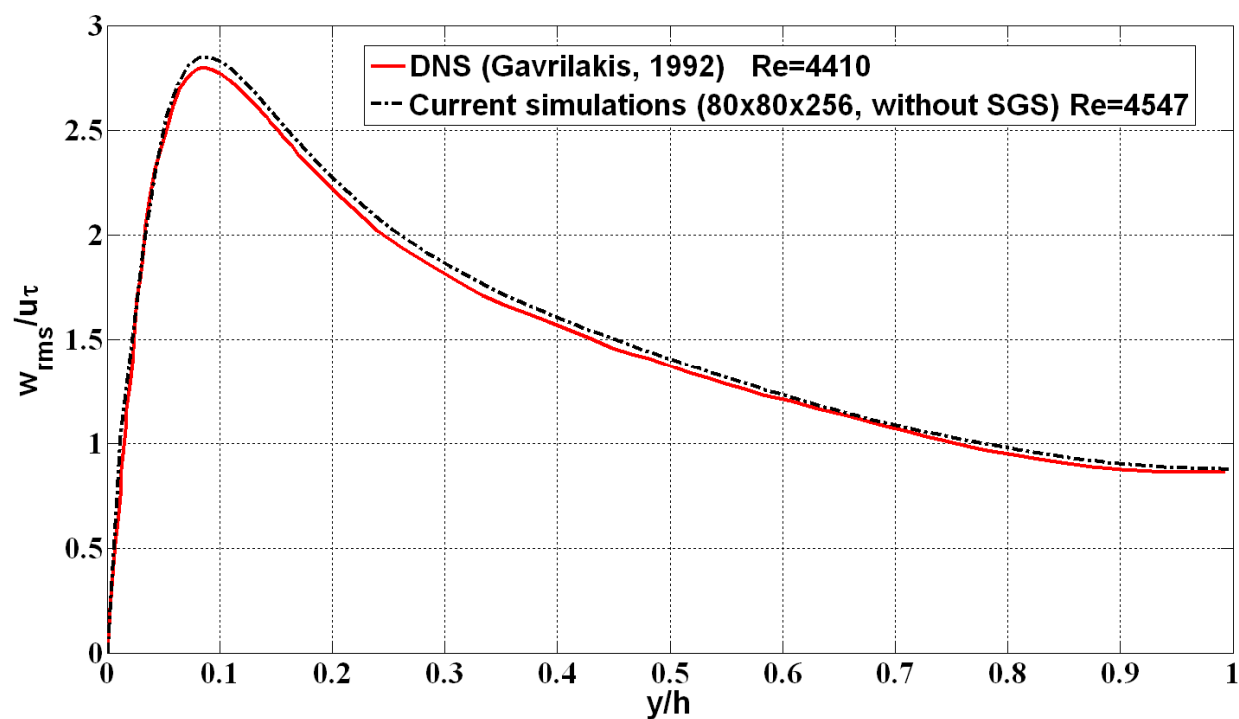


Fig. 5(c) Comparison of RMS of axial velocity fluctuations along vertical bisector with Gavrilakis [15]

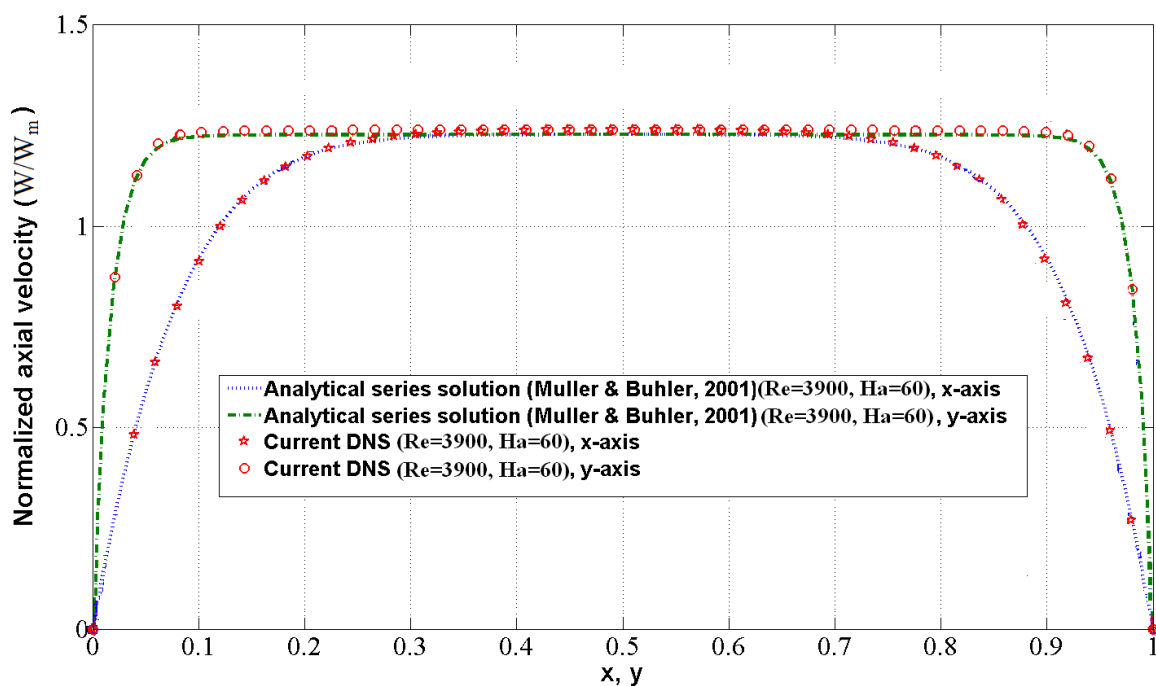


Fig. 6 Comparison of laminarized results (64x64x128) with Muller & Buhler [31]

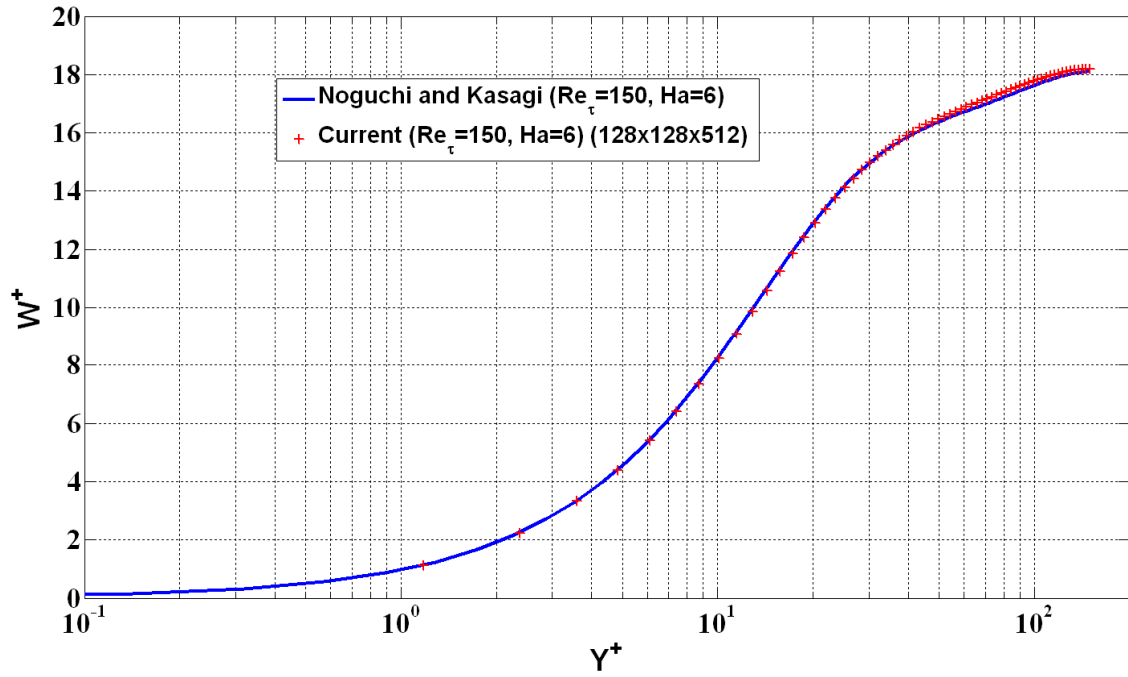


Fig. 7(a) Comparison of mean axial velocity in MHD channel at $Re_\tau=150$ and $Ha=6$ with Noguchi and Kasagi (1994) [26]

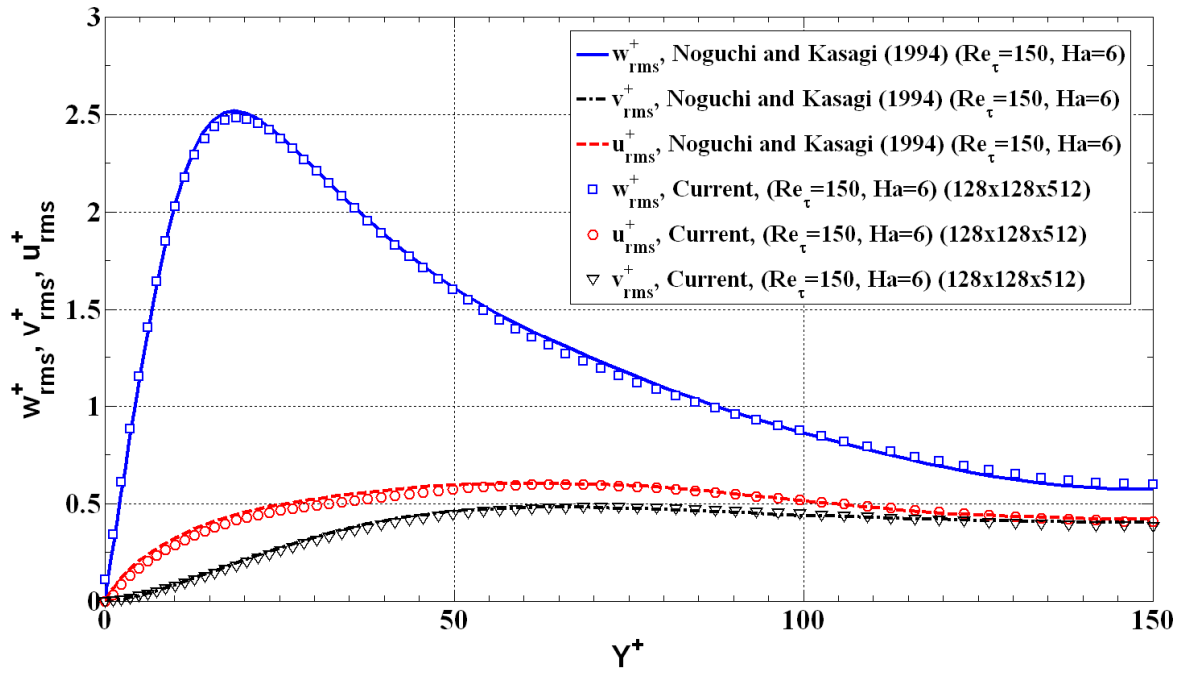


Fig. 7(b) Comparison of RMS of velocity fluctuations in MHD channel at $Re_\tau=150$ and $Ha=6$ with Noguchi and Kasagi (1994) [26]

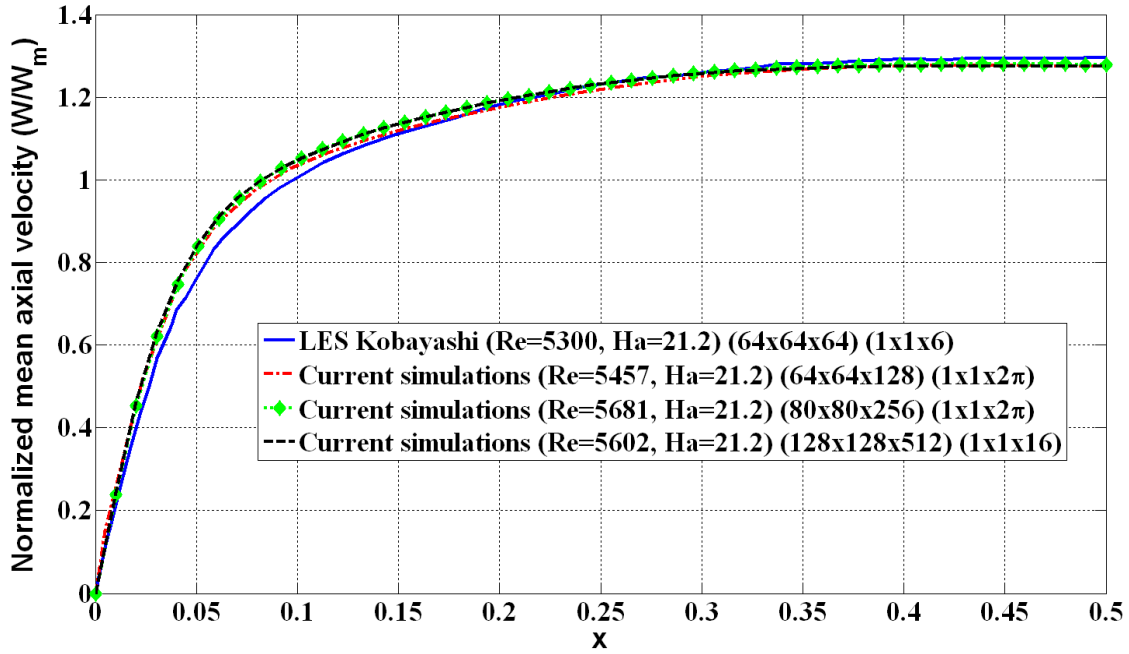


Fig. 8(a) Mean axial velocity along horizontal bisectors with Kobayashi (2008) [30] at $Ha=21.2$

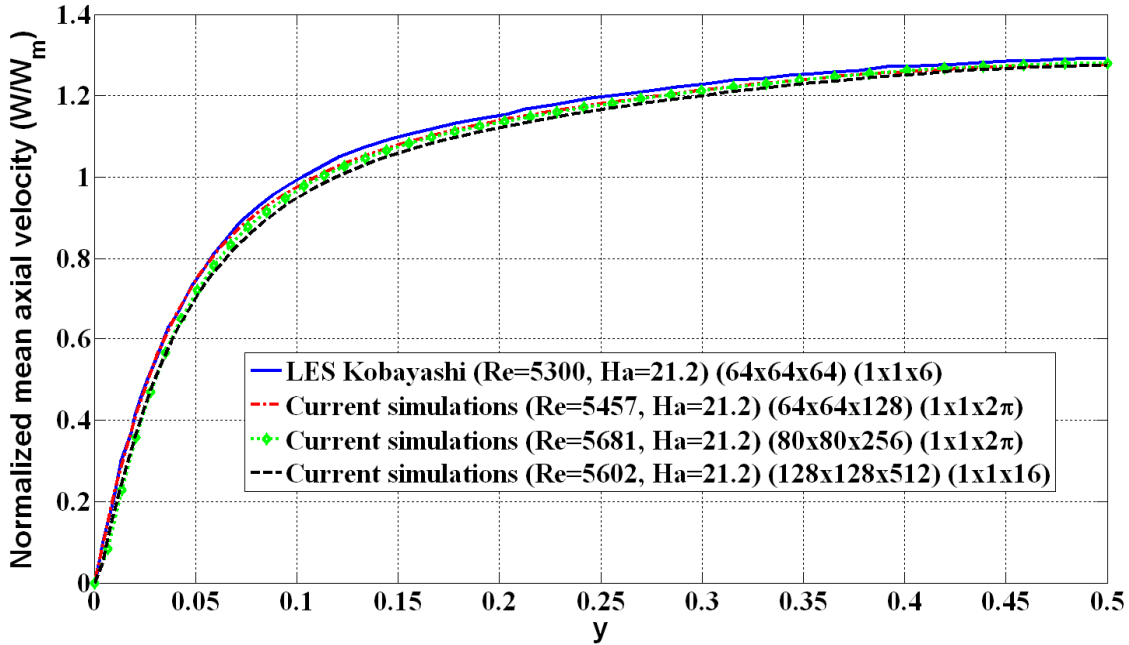


Fig. 8(b) Mean axial velocity along vertical bisectors with Kobayashi (2008) [30] at $Ha=21.2$

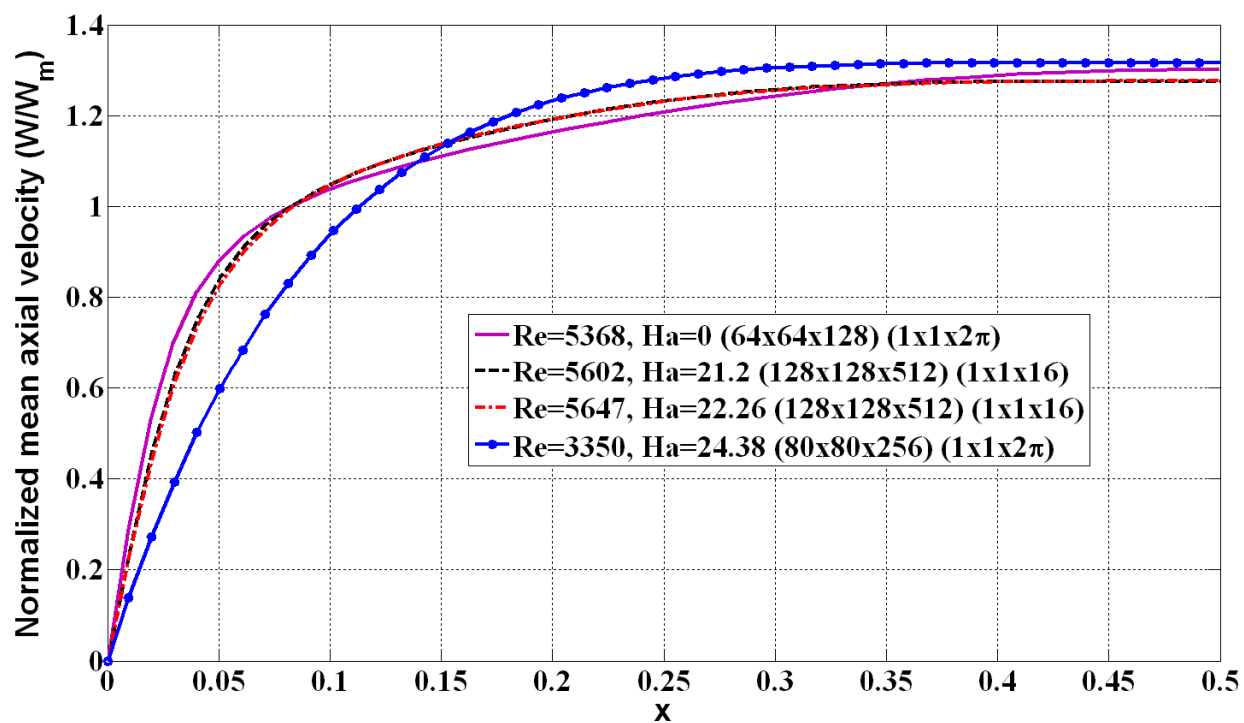


Fig. 8(c) Mean axial velocity along horizontal bisectors in various cases

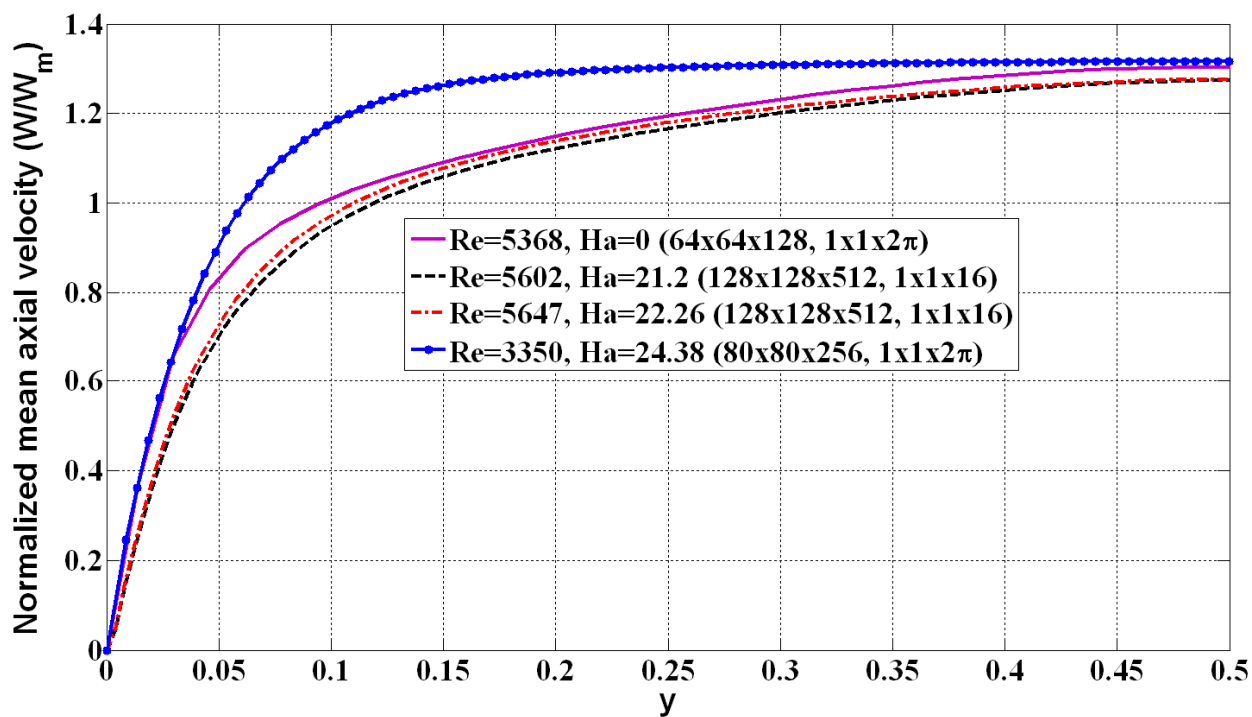


Fig. 8(d) Mean axial velocity along vertical bisectors in various cases

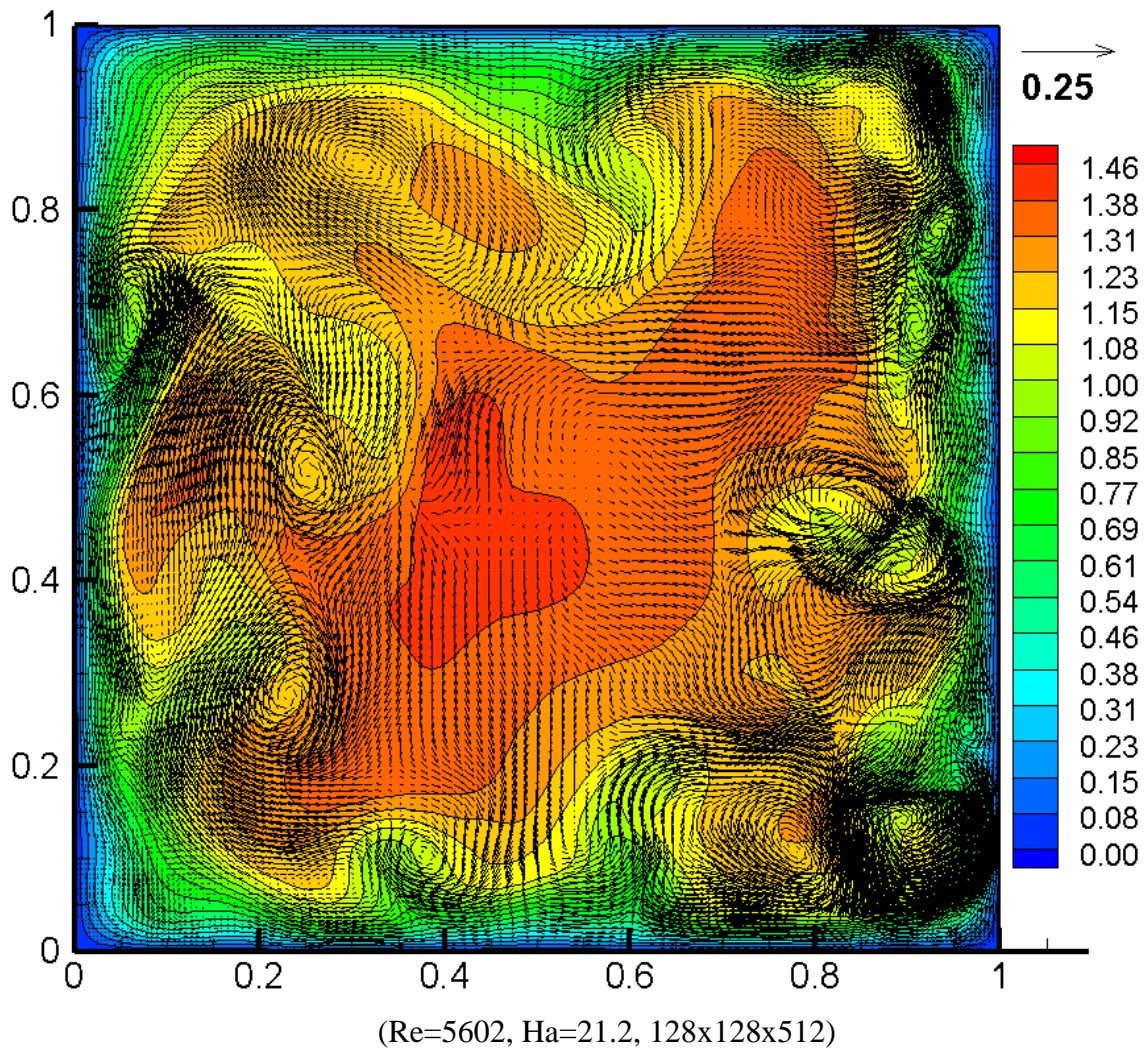


Fig. 9(a) Instantaneous axial velocity contours with secondary velocity vectors

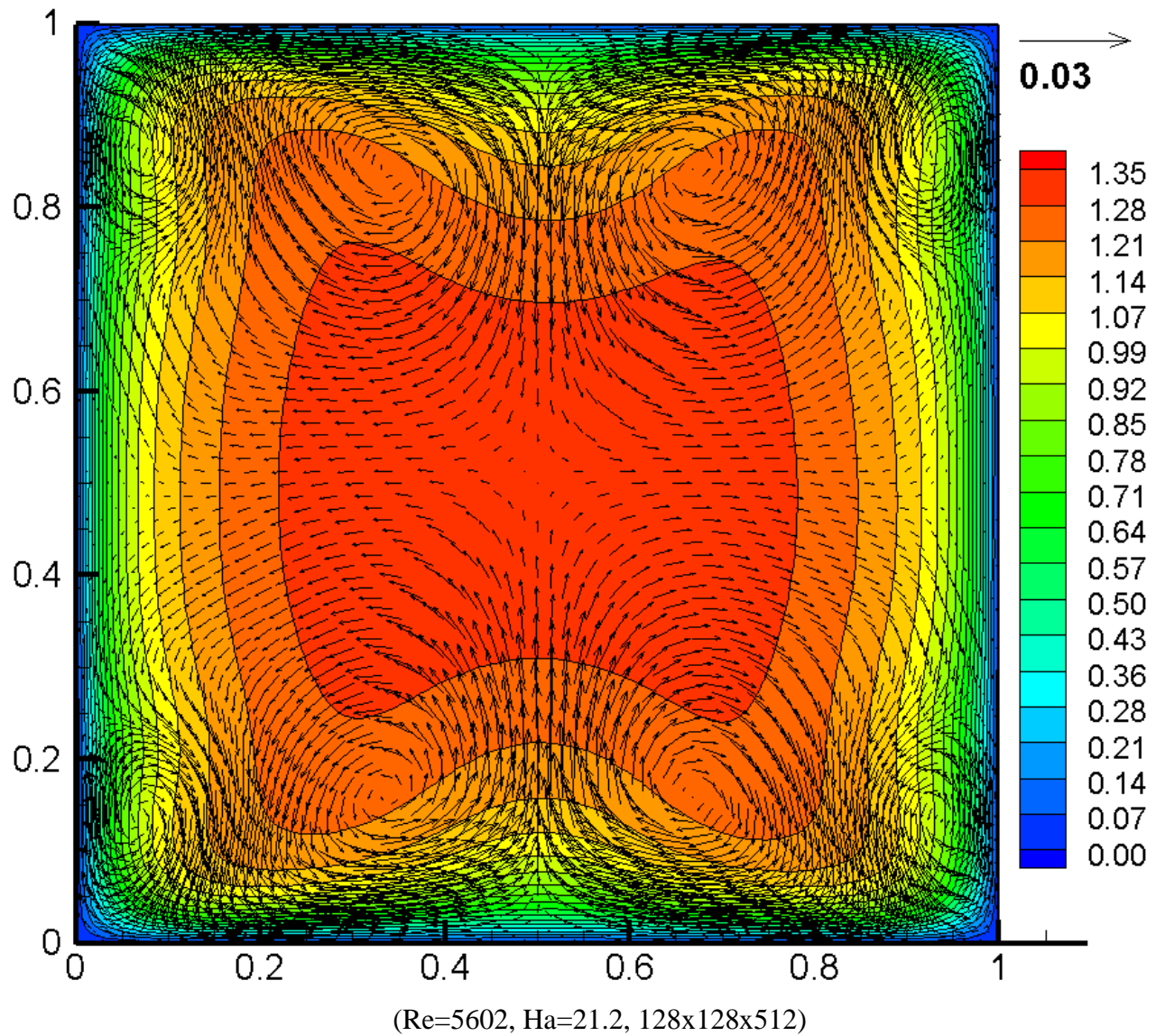


Fig. 9(b) Mean axial velocity contours with secondary velocity vectors.
(some vectors are skipped in mean secondary velocity for better visualization)

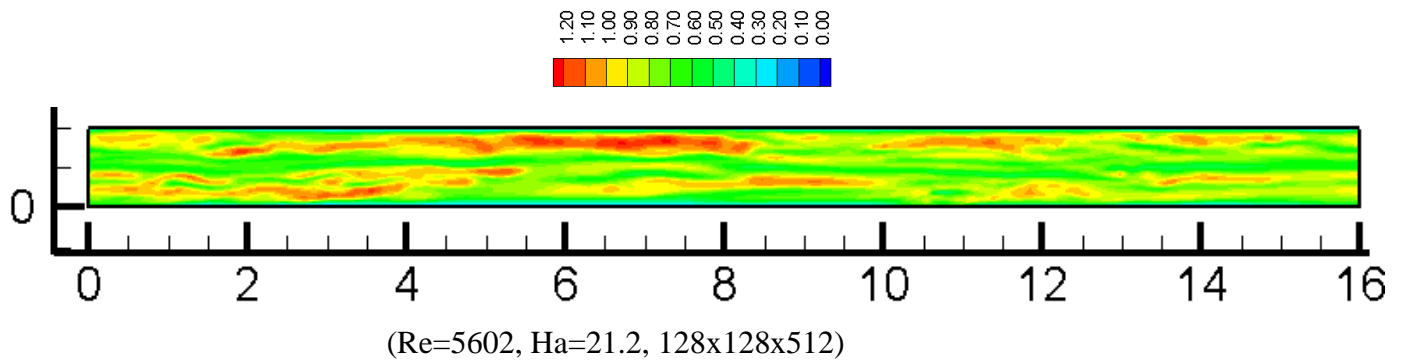


Fig. 9(c) Instantaneous velocity contours at $y^+=15$

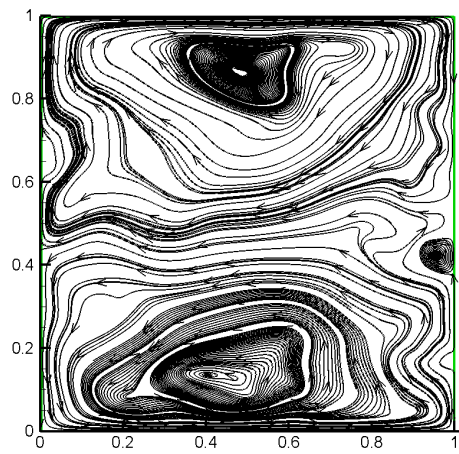
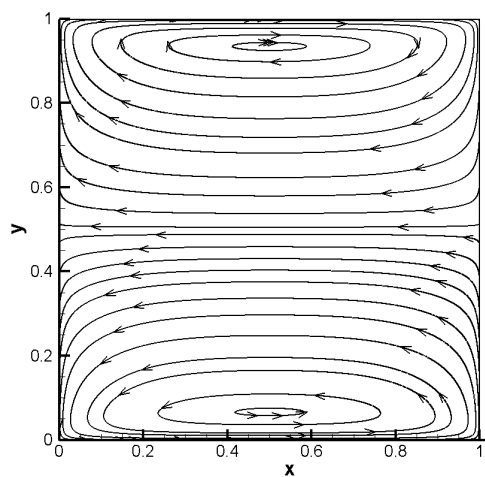


Fig. 9(d) Instantaneous induced current lines across a cross-section

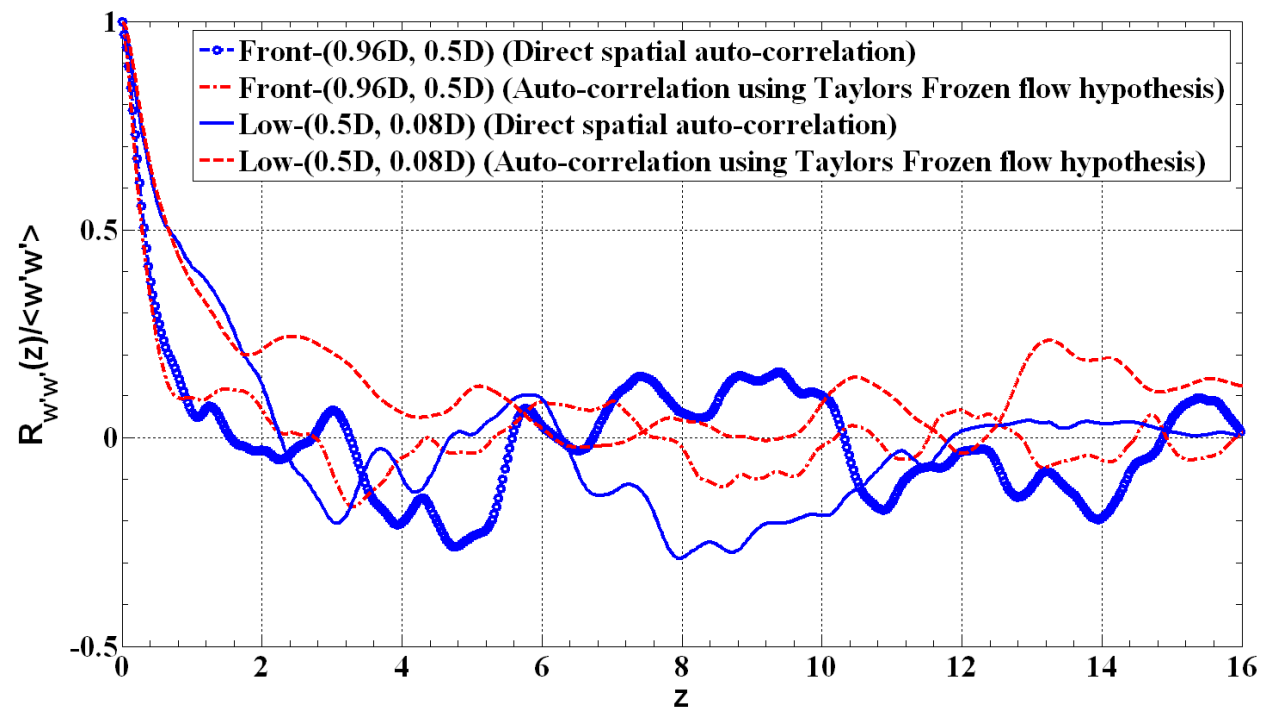


Fig. 10 Auto-correlation of axial velocity fluctuations (Re=5602, Ha=21.2)

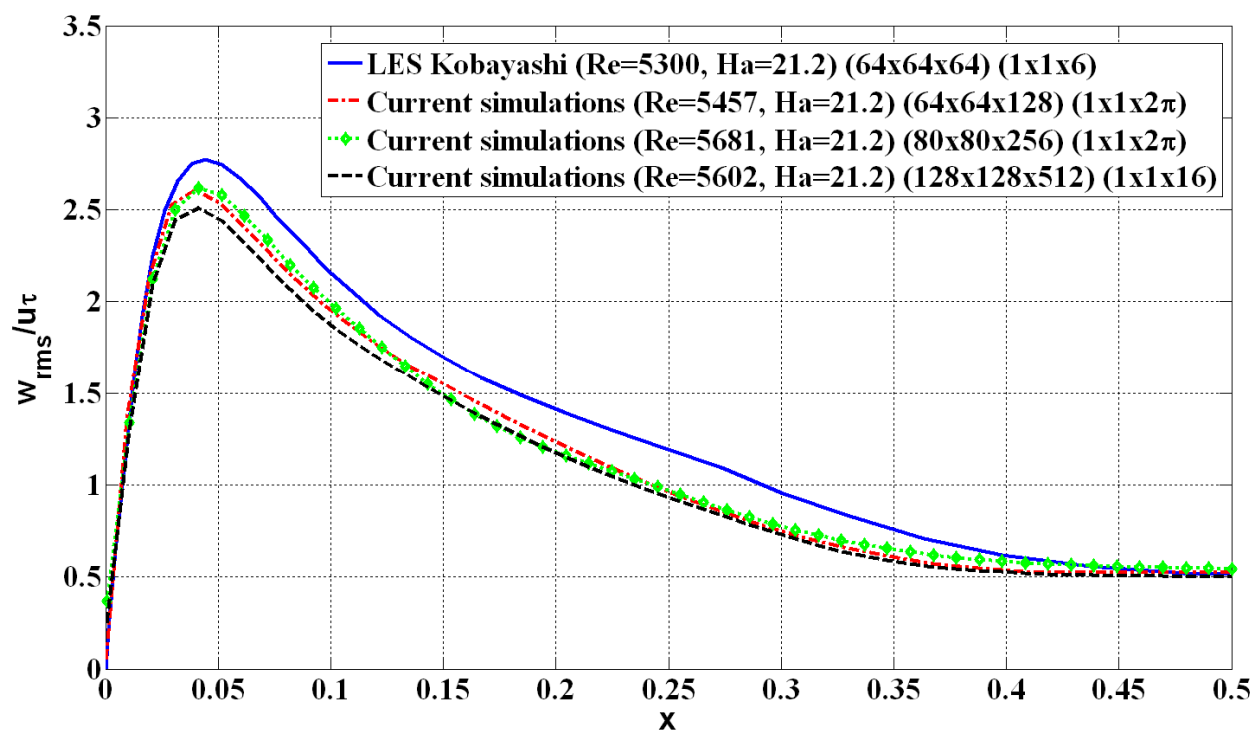


Fig. 11(a) RMS of axial velocity fluctuations along horizontal bisector

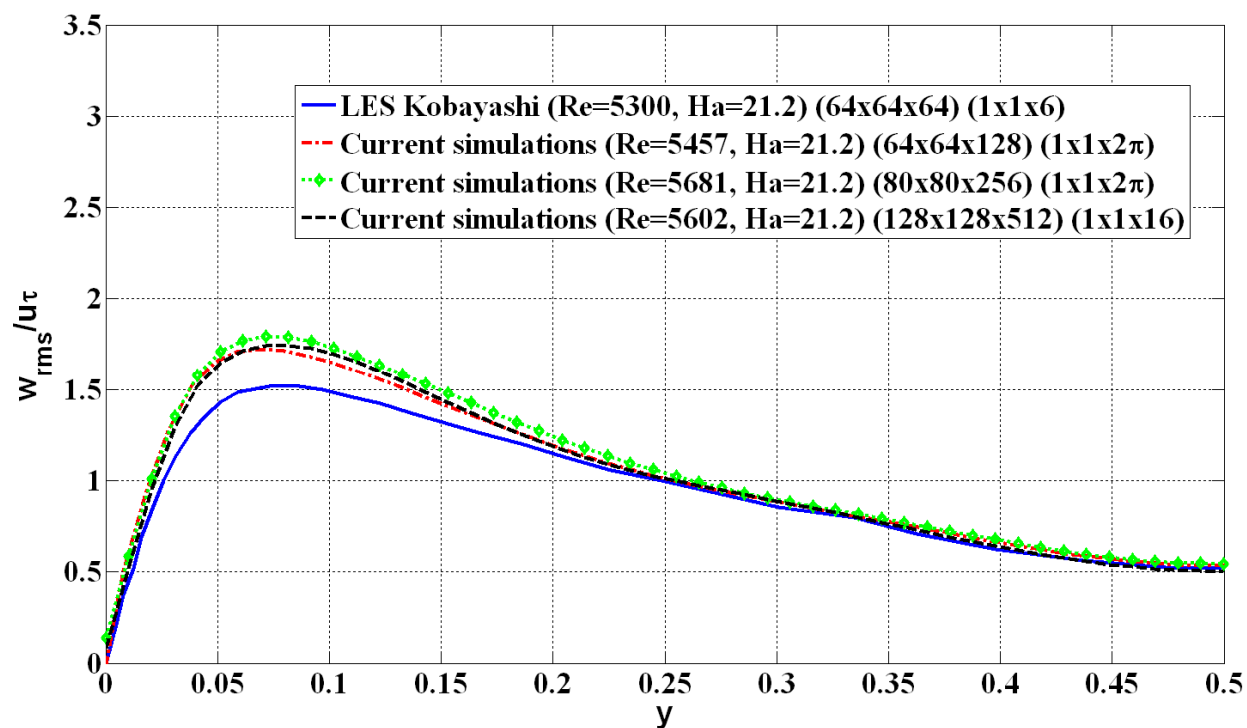


Fig. 11(b) RMS of axial velocity fluctuations along vertical bisector

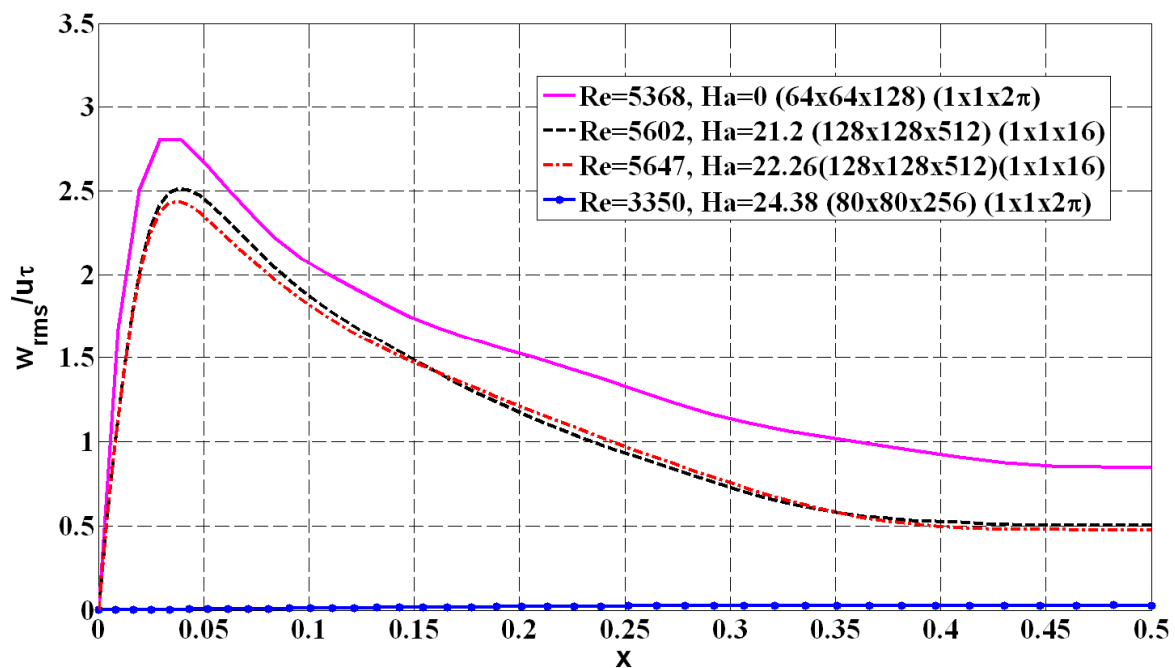


Fig. 12(a) RMS of axial velocity fluctuations along horizontal bisector for various Ha

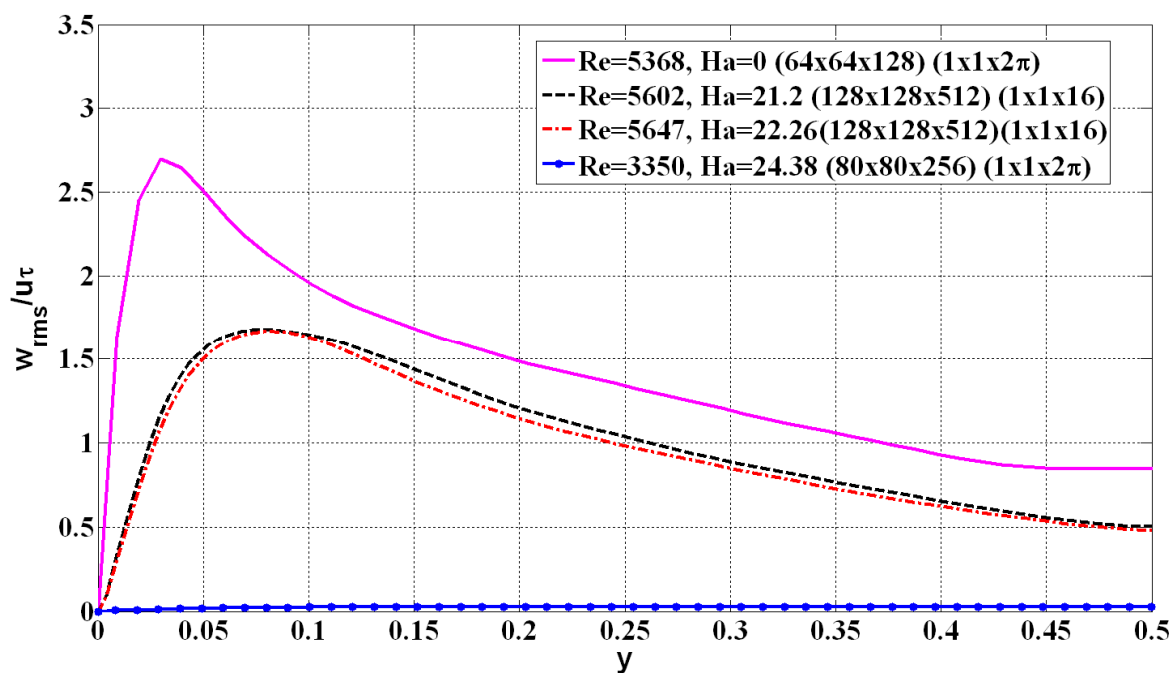


Fig. 12(b) RMS of axial velocity fluctuations along vertical bisector for various Ha

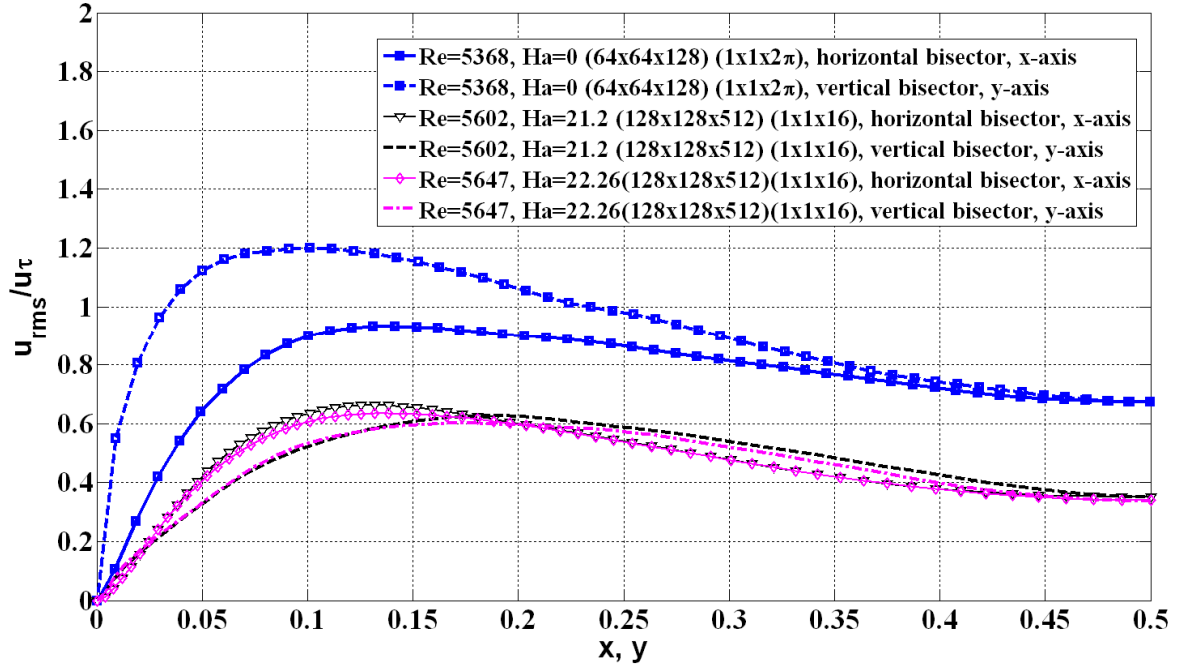


Fig. 13(a) RMS of horizontal velocity fluctuations along horizontal(x-) and vertical(y-) bisectors

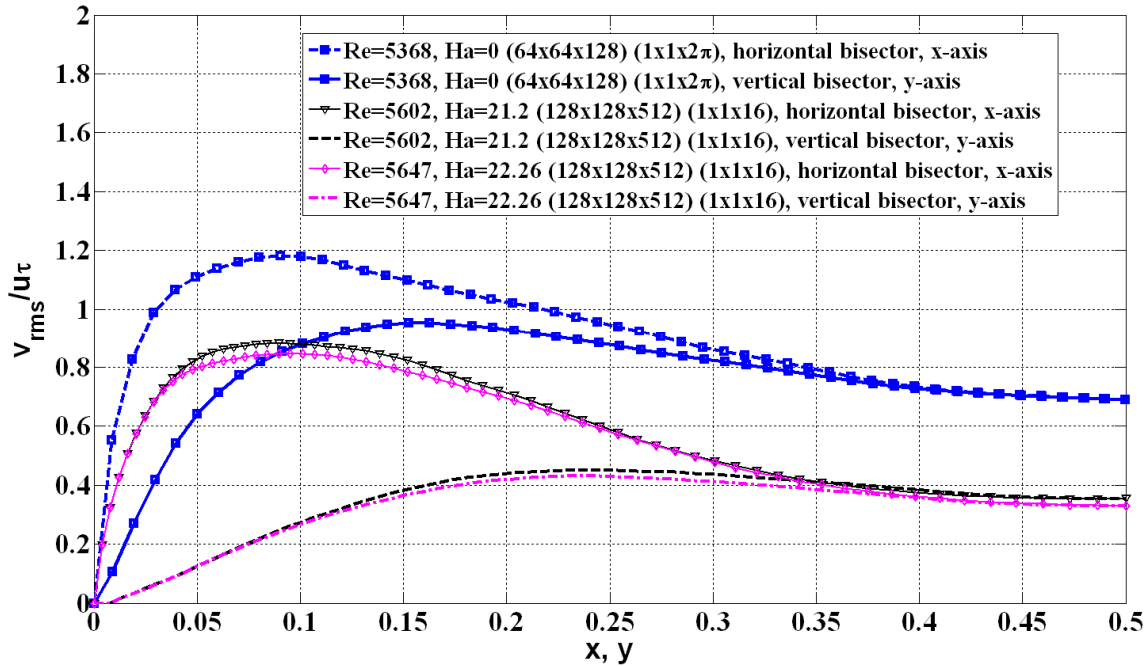


Fig. 13(b) RMS of vertical velocity fluctuations along horizontal(x-) and vertical(y-) bisectors

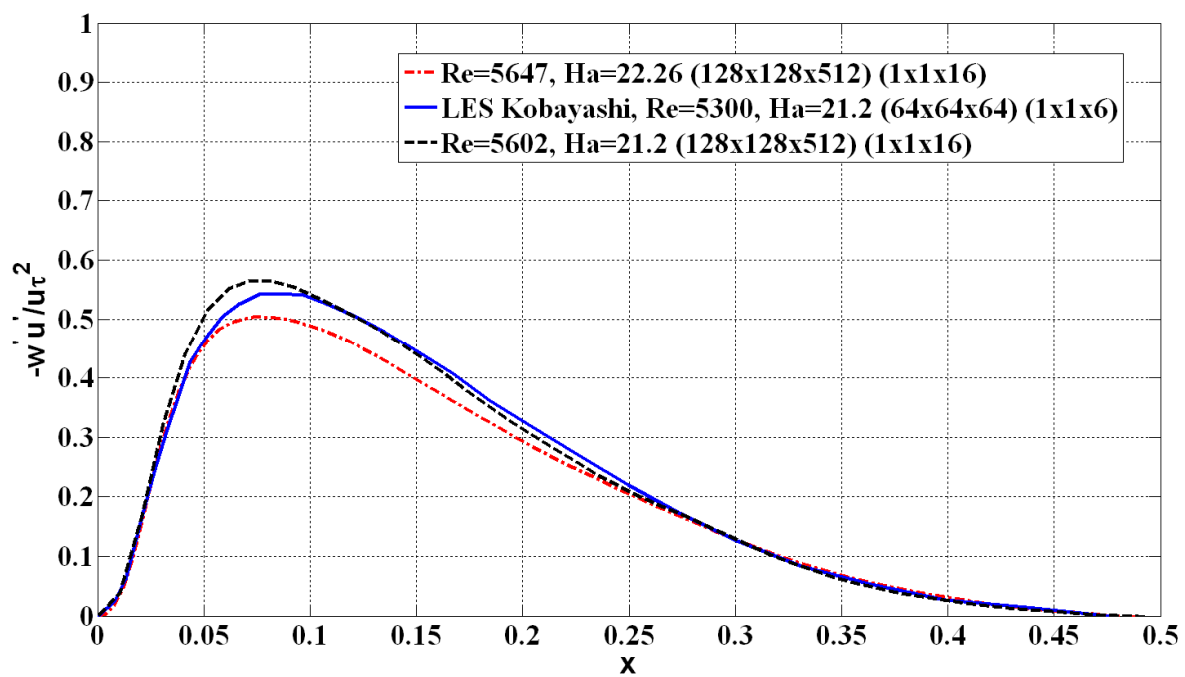


Fig. 14(a) Reynolds shear stress along horizontal(x-) bisector

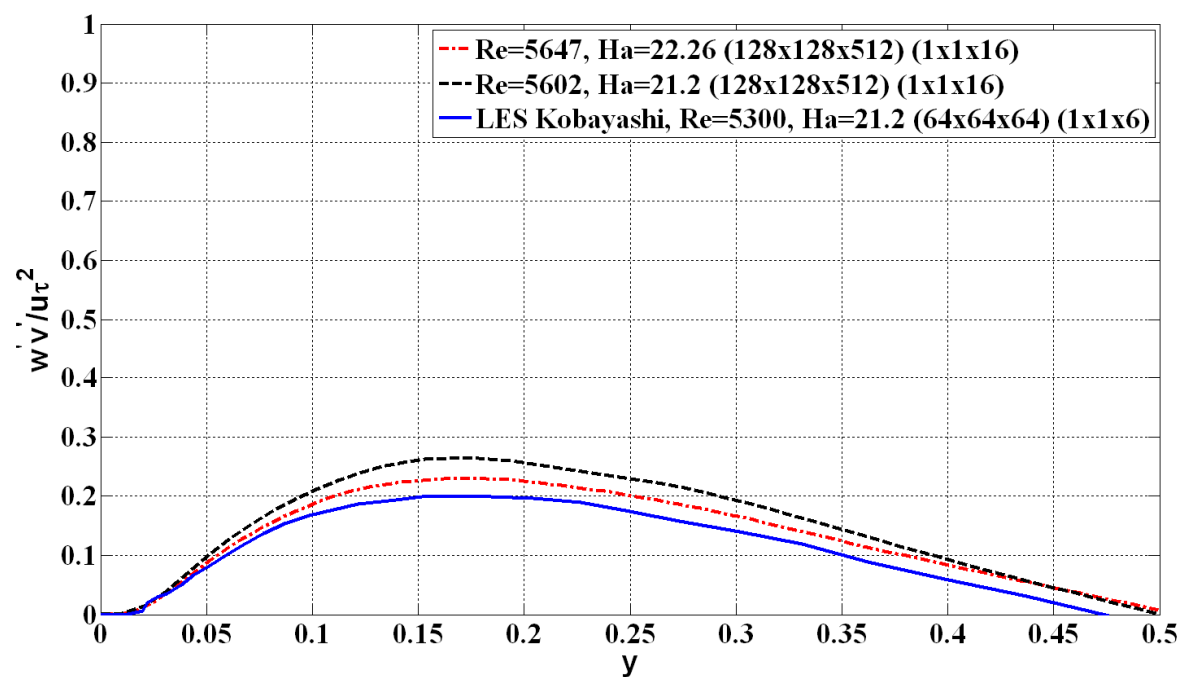


Fig. 14(b) Reynolds shear stress along vertical(y-) bisector

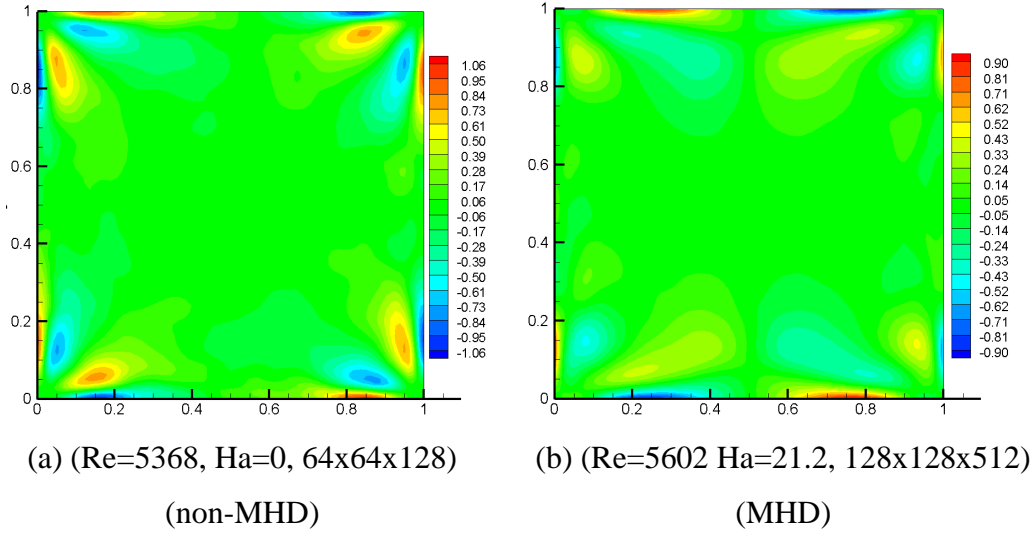
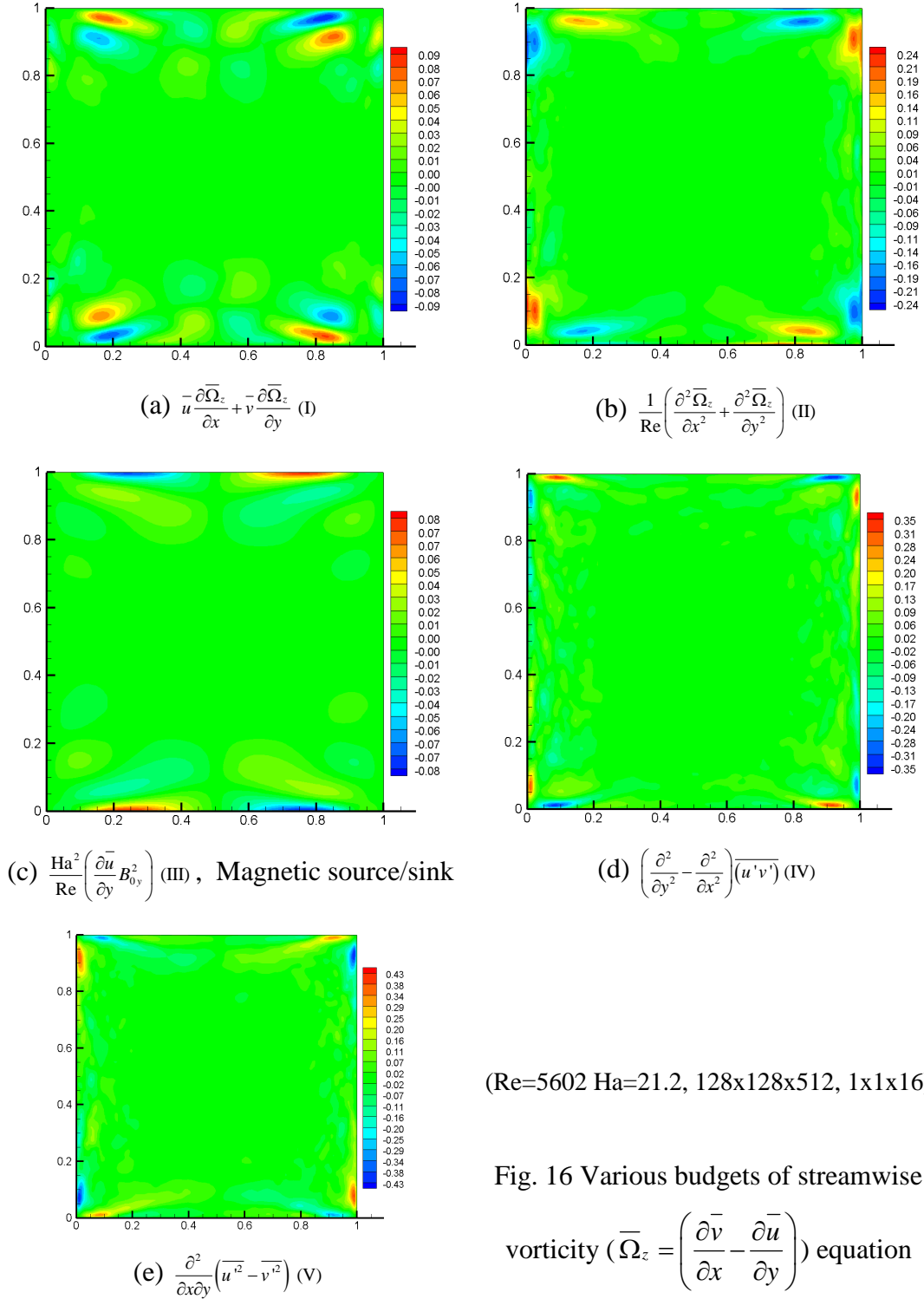


Fig. 15 Mean streamwise vorticity, $\bar{\Omega}_z = \left(\frac{\partial \bar{v}}{\partial x} - \frac{\partial \bar{u}}{\partial y} \right)$



(Re=5602 Ha=21.2, 128x128x512, 1x1x16)

Fig. 16 Various budgets of streamwise

vorticity ($\bar{\Omega}_z = \left(\frac{\partial \bar{v}}{\partial x} - \frac{\partial \bar{u}}{\partial y} \right)$) equation

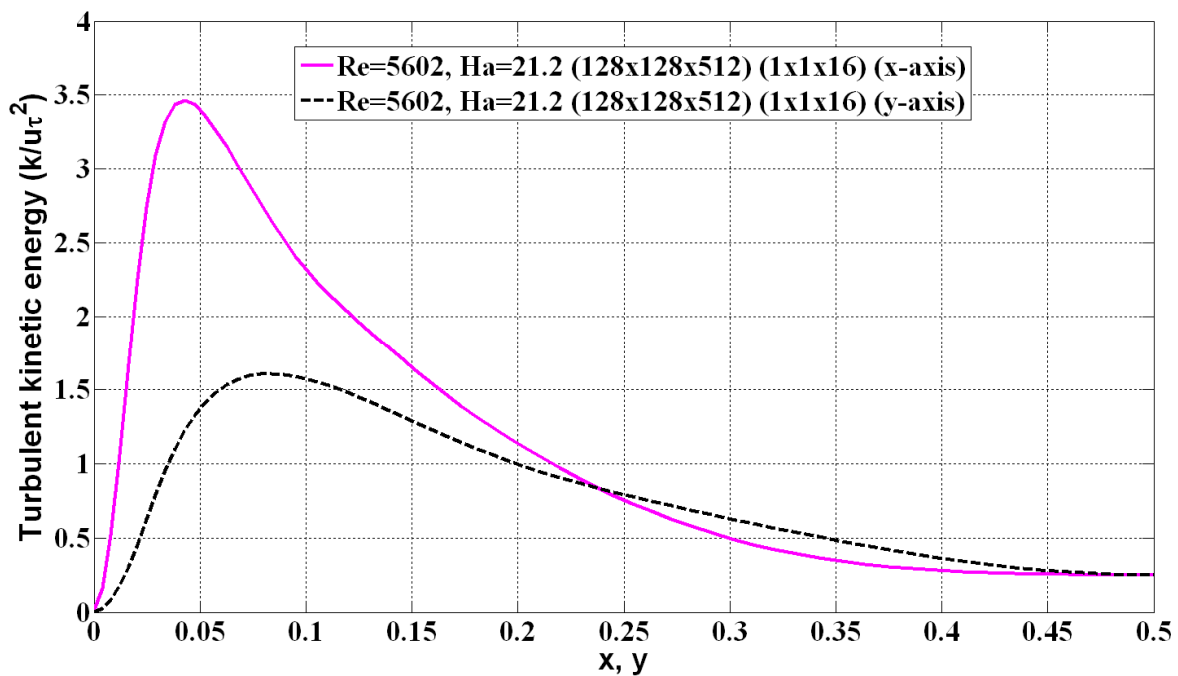


Fig. 17 Turbulent kinetic energy along horizontal (x-) and vertical (y-) bisectors

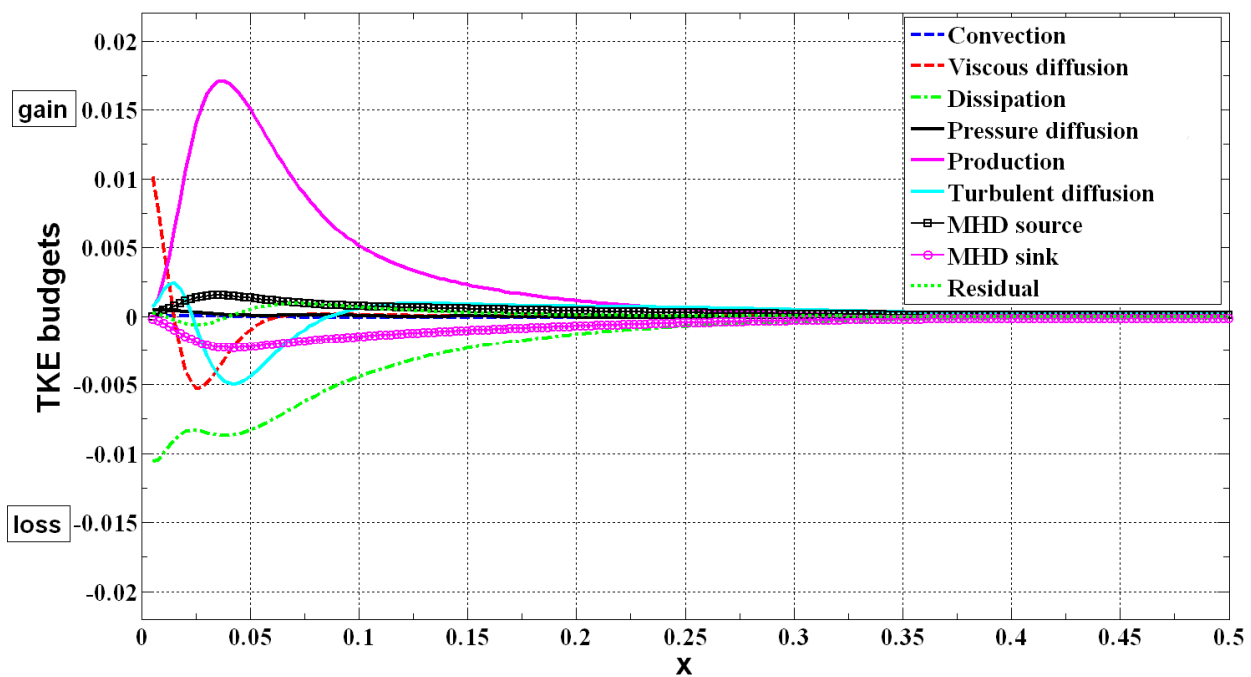


Fig. 18(a) TKE Budgets along horizontal(x-) bisector

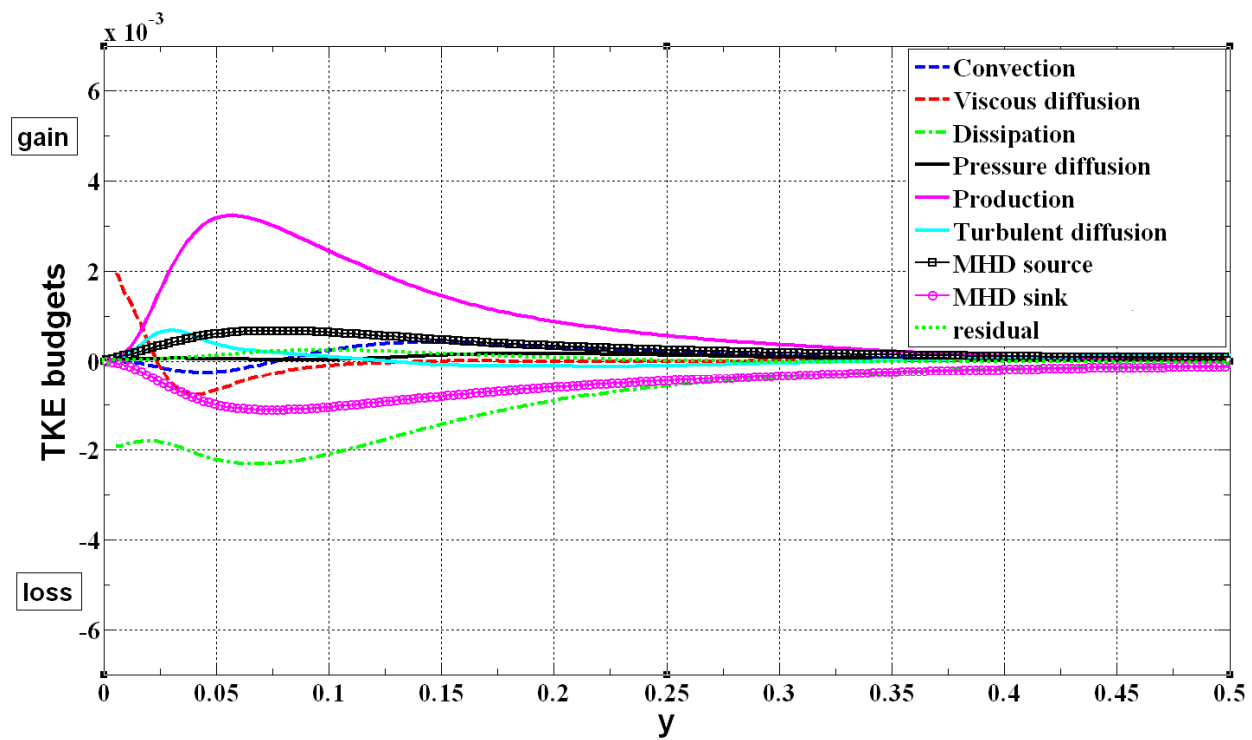


Fig. 18(b) TKE Budgets along vertical(y-) bisector